JTRF2014: Analysis, Results and Comparisons to ITRF2014 and DTRF2014

Claudio Abbondanza[1], Toshio Michael Chin[1], Richard S. Gross[1], Michael B. Heflin[1], Jay W. Parker[1], Benedikt S. Soja[1], Tonie M. van Dam[2], Xiaoping Wu[1]

[1] *Jet Propulsion Laboratory, California Institute of Technology, Pasadena, California, USA*
[2] *Faculté des Sciences, de la Technologie et de la Communication, Université du Luxembourg, L-1359 Luxembourg*

Abstract. We review the main steps that led to the construction of JTRF2014, the frame solution the Jet Propulsion Laboratory (JPL) submitted for the realization of ITRF2014. In the first part of this technical note, we recall the main concepts underlying the determination of terrestrial reference frames through Kalman Filtering and Rauch-Tung-Striebel smoothing, currently adopted at JPL to compute sub-secular frame products, and we discuss the main results associated with JTRF2014. In the second part, we adopt a comparative approach and, elaborating on metrics associated with Earth Orientation and Helmert transformation parameters, we analyze JTRF2014 in relation to ITRF2014, the official combined frame computed at the Laboratoire de Recherche en Géodésie of the Institut National de l'Information Géographique et Forestière (IGN) and DTRF2014, produced at the Deutsches Geodätisches Forschungsinstitut of the Technische Universität München.

Introduction

We present and discuss JTRF2014, the Terrestrial Reference Frame (TRF) the Jet Propulsion Laboratory constructed by combining space-geodetic inputs from Very Long Baseline Interferometry (VLBI), Satellite Laser Ranging (SLR), Global Navigation Satellite Systems (GNSS) and Doppler Orbitography and Radiopositioning Integrated by Satellite (DORIS) submitted for the realization of ITRF2014. Determined through a Kalman filter and RTS smoother assimilating position observations, Earth Orientation Parameters (EOPs), and local ties, JTRF2014 is a sub-secular, time series-based TRF whose origin is at the quasi instantaneous Center of Mass (CM) as sensed by SLR and whose scale is determined by the quasi instantaneous VLBI and SLR scales. JTRF2014 is rotationally aligned to ITRF2008 through the implementation of a No-Net-Rotation (NNR) condition applied at each step of the filter.

The kinematic evolution of the station positions is described by superimposing a secular motion, annual, and semi-annual periodic modes. Site-dependent variances based on the analysis of loading displacements induced by mass redistributions of terrestrial fluids have been used to control the extent of random walk adopted in the combination.

This technical note is conceptually articulated in two parts: The first recalls the main concepts underlying the JPL approach to TRF combination and illustrates the main products associated with JTRF2014;

the second dwells upon the comparative analyses of JTRF2014 in relation to ITRF2014, the official combined frame computed at the Laboratoire des Recherche en Géodésie (LAREG) of the Institut National de l'Information Géographique et Forestière (IGN) and to DTRF2014 produced at the Deutsches Geodätisches Forschungsinstitut (DGFI) of the Technische Universität München (TUM).

JTRF2014 Input Data

Between July 2015 and June 2016 entirely reprocessed global solutions from IVS, ILRS, IGS, and IDS roughly spanning the time window 1980–2015 were submitted to the IERS combination centres for the creation of ITRF2014.

Complying with the IERS-ITRF specifications, the SG global solutions are time series of Solution INdependent EXchange Format (SINEX) files containing integrated station positions at different temporal resolutions as well as daily EOP observations with full covariance matrices.

Table 1 reports the main features of the newly reprocessed SG inputs and lists recently published references wherein a thorough discussion on the nature of the solutions can be found. Prior to the combination with KALREF, the SG inputs were pre-processed, edited and pre-analysed.

Pre-processing

Since KALREF assimilates input data in the form of minimally constrained SG solutions [34], the pre-processing entails transforming the solutions into KALREF-compliant inputs.

Session-wise VLBI Normal Equations (NEQs) were inverted by applying No-Net-Translation (NNT) and No-Net-Rotation (NNR) conditions to the a-priori station coordinates supplied in the input SINEX files.

SLR inputs being loosely constrained solutions, their covariance matrices were orthogonally projected over rotations as shown in [7]. To allow for a faster data assimilation, repro2 (GNSS) daily solutions were averaged to weekly inputs. In so doing, each aggregated SINEX file contains weekly integrated station positions and seven daily EOPs, i.e. polar motion (x_p, y_p), polar motion rates $(\dot{x}_p, \dot{y}_p)$, and the calibrated excess length-of-day.

Data Editing

Data editing is mainly concerned with the identification and removal of position outliers. Outlier detection is based upon single-technique intrinsic stacks of pre-processed input SINEX files. Adopting the approach outlined by [1], secular frames were estimated from each individual SG time series of input SINEX files and residuals were computed with respect to the model

$$X^S(t) = X_0^C + V^C \cdot (t - t_0) + T(t) + \lambda(t) \cdot X_0^C + \mathbf{R}(t) \cdot X_0^C \quad (1)$$

where $X^S(t)$ is the vector defining the technique-specific position observations at the epoch t, the pair (X_0^C, V^C) represents the secular frame, i.e. the position vector at the reference epoch t_0 and the velocity vector; $\lambda(t)$, $T(t)$, and $\mathbf{R}(t)$ are the radial scale, the $3D$ translation vector and the anti-symmetric matrix of the $3D$ infinitesimal rotations about the coordinate axes at the epoch t, respectively.

Any observation having normalized and non-normalized residuals larger than the specified thresholds (cf Table 2) in any of three North, East and Height components has been flagged and removed from the input SINEX files. The stack and subsequent outlier removal have been iterated thrice for each technique. After each iteration, VLBI and SLR edited SINEX files have been screened for regional sessions. A SINEX file is regarded as regional when the area of the observing SG network covers an extremely limited portion of the globe. SG sessions having spherical area smaller than $2 \cdot 10^{12}\ m^2$ (Europe has an area of approximately $10^{13}\ m^2$) are classified as regional. Regional SG sessions are not able to convey reliably global Helmert transformation parameters which are pivotal in the definition of combined TRFs. Particularly affected in this regard appears to be the VLBI radial scale related to regional sessions. Whenever a regional sessions is detected, its corresponding SINEX file gets removed. Table 2 features the edited SG inputs adopted in JTRF2014.

The JTRF2014 Global Network

The JTRF2014 SG network consists of 972 stations, 671 of which are GNSS, VLBI and SLR count 71 stations each, whereas DORIS 159 (cf Table 2).

The color-coded map in Figure 1 represents the spatial distributions of the SG stations. With 453 sites in the Northern hemisphere against 137 site in the Southern, the uneven site distribution is markedly evident. JTRF2014 adopts the smallest global network when compared to ITRF2014 (1499 stations) and DTRF2014 (1712 stations) both of which take advantage of the remarkably larger number of GNSS stations available in IGS repro2 [27].

Intrinsic Quality of the single-technique contributions to JTRF2014

Station position coordinates can be used to define a proxy for the frame internal precision so as to provide an indication of the intrinsic quality of the SG solutions contributing to JTRF2014. The post-fit residuals from the intrinsic stack of Equation 1 can be used to define across-stations, per-session weighted mean squared errors (WRMS). Details on the implementation of such metric can be found in [27]. The WRMS analyses conducted on the edited SG inputs to JTRF2014 proved substantially consistent with the most recent investigations reported in the literature [see e.g. 17, 27].

Table 1: *SG inputs submitted for the ITRF2014 combination. T in the first column designates the SG techniques, whose acronyms derived from the IERS Conventions (cf Chapter 4 of [19]) are extensively used throughout the manuscript: P identifies GNSS, R VLBI, L SLR whereas D is DORIS. TC in the second column identifies the Technique Center. TS in the third column designates the time span for each technique. SOL in the fourth column specifies the kind of SINEX format released by the 4 TCs: VC stands for Variance-Covariance, NE for Normal Equations. TR in the fifth column relates to the temporal resolution, SF in the sixth is the number of SINEX files for each solution. ST in the seventh column reports the number of stations. The last column Source provides references.*

T	TC	TS	SOL	TR	SF	ST	Source
P	IGS	1994.0 – 2015.1	VC	Daily	7714	1845	[27]
R	IVS	1979.5 – 2015.0	NE	Session-Wise	5796	158	[5]
L	ILRS	1983.0 – 1993.0	VC	Fortnightly	244	138	[16]
L	ILRS	1993.0 – 2015.1	VC	Weekly	1148	138	[16]
D	IDS	1993.0 – 2015.0	VC	Weekly	1139	160	[17]

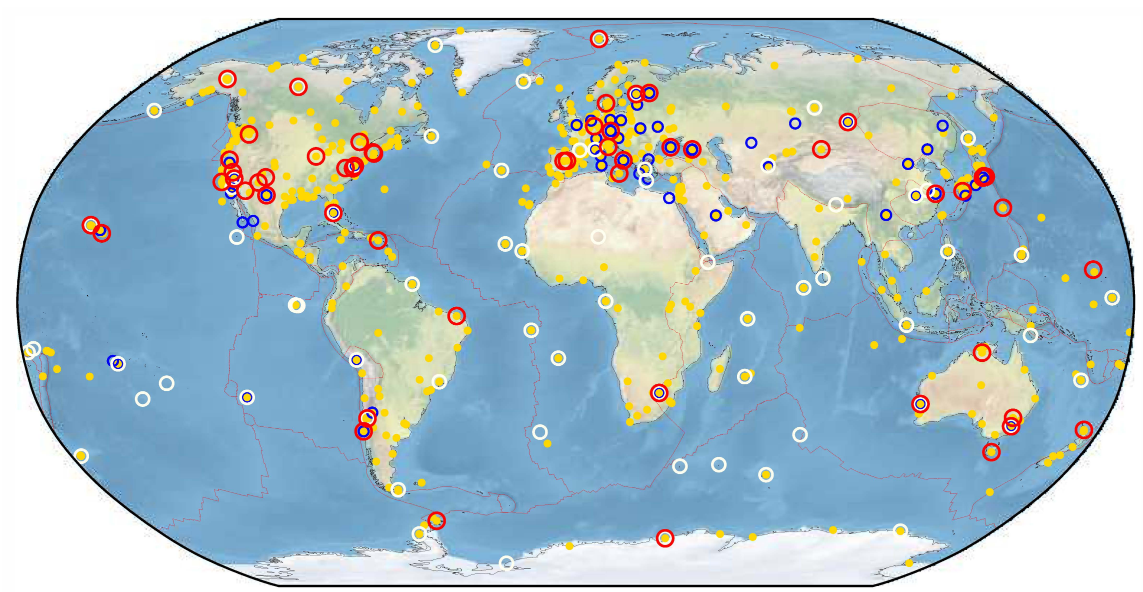

Fig. 1: *Global SG network adopted in the JTRF2014 combination. Gold dots identify the GNSS sites, red circles represent VLBI, the blue ones are SLR, whereas the white ones are DORIS. The global network comprises 671 GNSS stations, 71 VLBI and SLR stations, and 159 DORIS stations. The global network is characterized by 590 sites, 453 of which are located in the Northern hemisphere. Only 137 are positioned in the Southern hemisphere. Polygons drawn in red represent tectonic plate boundaries.*

Table 2: *Technique-specific thresholds adopted during the data editing of the input SINEX files. T in the first column identifies the SG technique, TC in the second one denotes the Technique Center, TR in the third one is the Temporal Resolution, the asterisk in the fourth column identifies the SG techniques subject to removal of regional sessions, OTS in the fifth column denotes the Observing Time Span threshold in yr applied to the stations, NR in the sixth column reports the Normalized Residual while AR defines the non-normalized Residual expressed in cm, STAT in the eighth designates the number of stations included in JTRF2014 and SNX in the last column denotes the number of SINEX files utilized in JTRF2014. Parenthesized in sixth column is the number of SINEX files removed over the entire time span of the combination as a result of the data editing illustrated in Section* Data Editing.

T	TC	TR	Regional	OTS	NR	AR	STAT	SNX
P	IGS	Weekly	–	2.5	5	5	671	1102 (-)
R	IVS	Session-Wise	*	2.5	7	5	71	4681 (1115)
L	ILRS	Fortnightly/Weekly	*	2.5	7	5	71	1293 (99)
D	IDS	Weekly	–	2.5	7	5	159	1139 (-)

As shown in Table 3, with median WRMS smaller than 4.4 mm on any of the three components, the weekly averaged GNSS solutions are by far the most precise, followed by VLBI, SLR and DORIS. When comparing median WRMS of SG inputs computed with consistent data editing procedures for the ITRF2008 data sets, we found a remarkable improvement for DORIS, whose station position repeatability decreases by ≈ 3 mm on each component and for SLR as well.

JTRF2014 Multi-technique Combination

KALman filter for terrestrial REference Frame (KALREF) combines minimally constrained SG inputs along with local tie observations through the adoption of a Kalman Filter and Rauch-Tung-Striebel (RTS) Smoother algorithm. While running forward in time, the filter produces optimal estimates of the state parameters of a certain epoch based on the observations assimilated up to that epoch. The fixed-interval RTS smoother is executed backward in time thus ensuring optimal state estimate based on all the measurements acquired over the entire data assimilation span.

Kinematic Model and Time Update

During the time and measurement update in the forward filtering stage, KALREF updates the set of variables describing the state of the dynamical system according to what is observed and what the physics of the dynamical model predicts. The dynamical model describes the temporal evolution of the prognostic parameters constituting the state vector. In KALREF, the state vector X_k consists of station-related parameters, such as the trend and seasonal variables describing the Earth surface deformation and network-related parameters, such as the EOPs and the Helmert transformation parameters. For the station-position related parameters, the dynamical model formulated adopting the state-space notation is

Table 3: *2nd-order statistics relevant to station positions and EOPs of the SG edited inputs. Station positions WRMS are across-station weighted root mean squared residuals computed through the linear model of Equation 1. Second, third and fourth columns report median values of the WRMS time series in mm for the North, East, and Height component, respectively. EOP WRMS reported in the following columns are weighted root mean squared residuals computed as a result of the intrinsic stack of the of the SG inputs. The fifth and sixth column report WRMS of the x and y components of the polar motion expressed in μas, respectively. Column 7 reports UT expressed in μsec. Column $8, 9$ and 10 relate to the polar motion rates $\dot{x_p}$, $\dot{y_p}$ and LOD expressed in $\mu as/day$ and $\mu sec/day$, respectively. The last column reports the square root of the reduced chi-square obtained as a result of the stacking of the edited input data sets. Parenthesized are the 2nd-order statistics computed for the input data sets adopted for the KALREF analysis of ITRF2008 [cf 38].*

T	Station Position			EOPs						s_0
	N	E	H	x_p	y_p	UT	$\dot{x_p}$	$\dot{y_p}$	LOD	
P	1.5 (1.6)	1.4 (1.4)	4.4 (4.2)	6.6 (1.3)	7.4 (1.3)	–	8.4 (9.3)	9.2 (12.0)	–	5.7 (0.9)
R	3.1 (3.3)	3.0 (2.9)	7.5 (7.2)	118.5 (160.5)	136.6 (179.8)	5.5 (6.3)	130.8 (132.2)	109.9 (133.6)	6.5 (5.2)	5.9 (5.5)
L	8.2 (10.1)	7.4 (9.2)	6.5 (7.8)	120.3 (168.2)	119.1 (168.5)	–	–	–	–	5.2 (4.4)
D	9.2 (10.8)	11.3 (13.6)	10.2 (13.3)	71.1 (58.8)	65.3 (68.5)	–	–	–	–	2.7 (3.2)

$$
\underbrace{\begin{bmatrix} x_k^{ij} \\ v_k^{ij} \\ s_k^{ij} \\ s_{k-1}^{ij} \\ q_k^{ij} \\ q_{k-1}^{ij} \end{bmatrix}}_{X_k}
=
\underbrace{\begin{bmatrix}
1 & \Delta t & 0 & 0 & 0 & 0 \\
0 & 1 & 0 & 0 & 0 & 0 \\
0 & 0 & 2e^{-\frac{\Delta t}{\tau}} \cos(\frac{2\pi\Delta t}{T_s}) & -e^{\frac{-2\Delta t}{\tau}} & 0 & 0 \\
0 & 0 & 1 & 0 & 0 & 0 \\
0 & 0 & 0 & 0 & 2e^{-\frac{\Delta t}{\tau}} \cos(\frac{2\pi\Delta t}{T_q}) & -e^{\frac{-2\Delta t}{\tau}} \\
0 & 0 & 0 & 0 & 1 & 0
\end{bmatrix}}_{\boldsymbol{\Phi}_k}
\cdot
\underbrace{\begin{bmatrix} x_{k-1}^{ij} \\ v_{k-1}^{ij} \\ s_{k-1}^{ij} \\ s_{k-2}^{ij} \\ q_{k-1}^{ij} \\ q_{k-2}^{ij} \end{bmatrix}}_{X_{k-1}}
+
\underbrace{\begin{bmatrix} \varepsilon_{x_k}^{ij} \\ \varepsilon_{v_k}^{ij} \\ \varepsilon_{s_k}^{ij} \\ 0 \\ \varepsilon_{q_k}^{ij} \\ 0 \end{bmatrix}}_{\mathcal{W}_k}
\quad (2)
$$

where

- the index $j = 1, 2, 3$ denotes the generic Cartesian component in the XYZ space,
- the index k identifies the epoch,
- Δt is the fixed time step set to 1 week,
- x_k^{ij} represents the non-periodic position of the station i at the epoch k,
- v_k^{ij} is the instantaneous velocity (trend variable),
- the triplets $\left(s_k^{ij}, s_{k-1}^{ij}, s_{k-2}^{ij}\right)$ and $\left(q_k^{ij}, q_{k-1}^{ij}, q_{k-2}^{ij}\right)$ are the elements of a second-order regression model discretizing the differential equation of a stochastic damped oscillator [10]: the former relates to the annual periodic mode, the latter to the semi-annual periodic mode;
- T_s and T_q designate the annual and semi-annual periods, respectively.

By setting the e-folding time τ to a large value, no damping is allowed in the harmonic oscillators. The state vector X_k is completed by 42 daily EOP parameters describing the Earth rotation (namely x_p, y_p, UT and their time derivatives $\dot{x}_p$, $\dot{y}_p$, LOD) for each day within the weekly interval and by Helmert transformation parameters grouped in sets each of which to be individually applied to the technique-specific global SG networks. $\mathbf{\Phi}_k$ designates the state-transition matrix allowing the state vector to be propagated from the epoch $k-1$ to k. In KALREF the state-transition matrix is time-invariant but the process- and measurement-noise covariance matrices are not. SG observing systems are uniquely able to sense the *total* station motion $\tilde{x}_k^{ij}$ defined through the following additive model:

$$\tilde{x}_k^{ij} = x_{k-1}^{ij} + v_{k-1}^{ij} \cdot \Delta t + s_k^{ij} + q_k^{ij} \tag{3}$$

Equation 3 accounts for all of elements into which the station motion has been decomposed and will be utilized during the measurement update described in the following section. Earth Orientation and Helmert transformation parameters are modeled as a pure random walk $h_k = h_{k-1} + \varepsilon_{h_k}$ where $\varepsilon_{h_k} \sim \mathcal{N}(0, \sigma^2)$ is a Gaussian process whose associated standard deviation σ is set to a value sufficiently large to accommodate the week-to-week variations observed in the Earth orientation and the Helmert parameters as well (cf Table 4).

The elements of the vector $\mathcal{W}_k$ relate to the stochastic nature of the state vector parameters, whose associated process noise is modeled as white-noise driven random walk. KALREF enables process noise to be activated on each of the state vector parameters, although in current TRF reductions process noise is solely turned on for station positions, EOPs and Helmert transformation parameters. By setting the variances of the Gaussian processes $\varepsilon^i_{v_k}$, $\varepsilon^i_{s_k}$ and $\varepsilon^i_{q_k}$ of Equation 2 to non-zero values, velocities and seasonal terms are allowed to stochastically vary in time, thus accommodating time-variable trends and amplitudes/phases of the seasonal oscillators [10]. The filter is initialized by utilizing the a priori values specified in Table 4, along with the uncertainties adopted to fill the diagonal terms of the covariance matrix at the first step of the assimilation.

Table 4: *Set-up adopted for the filter initialization: initial values of the state parameters as well as of the uncertainties adopted in the first step of the filter are reported in Column* 3 *(a priori state values) and Column* 4 *(a priori state uncertainties). Process noise for the state parameters is selected to be random walk driven by white noise, whose variance square roots are reported in Column* 5. *Column* 6 *defines the units adopted in the computational code (KALREF).*

Parameter	Description	a priori Value	Uncertainty	Process Noise σ	Units
x_k	Non-periodic Coordinates	$^{(a)}$	2	$^{(b)}$	m
v_k	Station Velocities	0	2	0	m/yr
s_k	Periodic Displacements	0	5	0	cm
x_p,y_p	Polar Motions	0	400	100	mas
$\dot{x}_p$,$\dot{y}_p$	Polar Motion Rates	0	400	100	mas/day
UT	Universal Time	0	400	100	ms
LOD	Excess Length-of-Day	0	400	100	ms/day
T	Translations	0	2	1	m
λ	Radial Scale	0	20	1.6	0.1·ppm
R	Rotations	0	200	3.2	$0.01 \cdot as$

$^{(a)}$ a priori station coordinates are derived from the first observed station coordinates in the time series.

$^{(b)}$ Station-dependent standard deviations of the position process noise are derived from the reduction of the UniLu-GGFC loading displacements as described in Section *Loading Models*.

Measurement Update

During the measurement update the a priori state estimates obtained by forward projecting the kinematic model are adjusted by minimizing the misfits between the physical model and the station position and EOP observations. The observation equations involved in the measurement update have therefore to establish a bijective relationship between the observed entities in the measurement space and the state parameters. The linearized Euclidean similarity transformation adapted from [1] can be used to construct the rank-deficient linear system of Equations central to KALREF measurement update:

$$\begin{cases} X_P^S = & X_P^C + T_P + \lambda_P X_P^C + \mathbf{R_P} X_P^C \\ X_R^S = & X_R^C + T_R + \lambda_R X_R^C + \mathbf{R_R} X_R^C \\ X_L^S = & X_L^C + T_L + \lambda_L X_L^C + \mathbf{R_L} X_L^C \\ X_D^S = & X_D^C + T_D + \lambda_D X_D^C + \mathbf{R_D} X_D^C \end{cases} \tag{4}$$

where

- X_t^S and X_t^C are vectors whose elements are the technique-specific total coordinates described in Equation 3. The index t represents the SG technique where P stands for GNSS, R for VLBI, L for SLR and D for DORIS;
- X_t^S relates to the weekly/daily input SINEX files station positions;
- X_t^C to the weekly combined (outputted) station positions;
- T_t denotes the vector of the translations mapping the combined frame XC to the pseudo-observed technique-specific XSt frame;
- λ_t denotes the radial scale factor between the combined and the technique-specific frames;
- $\mathbf{R_t}$ is the antisymmetric matrix representing a 3D linearized rotation between the combined and the technique-specific frames.

Note that, since small station position motions at sub-weekly time scale are being ignored, the time dependency in Equations 4 is dropped. The system of Equations 4 is complemented by EOP measurement equations relating the combined and observed Earth rotation to the Helmert rotation parameters:

$$\begin{cases} x_{t,p} = & x_p^C + r_{t,2} \\ y_{t,p} = & y_p^C + r_{t,1} \\ UT_t = & UT^C - \frac{1}{f} r_{t,3} \\ \dot{x}_{t,p} = & \dot{x}_p^C \\ \dot{y}_{t,p} = & \dot{y}_p^C \\ LOD_t = & LOD^C \end{cases} \tag{5}$$

where

- the subscript t denotes the Earth Orientation (Helmert rotational) parameters as observed by (determined through) the SG technique t;
- the superscript C denotes the combined EOP parameters included in KALREF state vector;
- (x_p, y_p) denotes the daily polar motion;
- $(\dot{x}_p, \dot{y}_p)$ denotes the daily polar motion rate;
- UT denotes the difference $(UT1 - UTC)$;
- LOD is the excess length of day representing discrete variations of UT over one day;
- (r_1, r_2, r_3) represent clockwise infinitesimal rotation angles about the X, Y and Z axes, respectively;
- $f = 1.002737909350795$ is the conversion factor from UT into sidereal time.

During the measurement update the technique-specific EOPs are simultaneously calibrated with the TRF rotational parameters so as to compensate for EOP-related systematic biases. In JTRF2014, polar motion observations from VLBI, SLR, GNSS and DORIS, polar motion rates from VLBI and GNSS, UT and LOD from VLBI are assimilated. The satellite-derived LOD, though available, has not been utilized in our combination in order to avoid potential corruption of VLBI-determined LOD [25].

The measurement equations are completed by the additive model of Equation 3 described in Section *Measurement Update*. The observations of position and EOPs fed into KALREF are weighted through the inverse of the measurement (full) covariance matrices reported in the input SINEX files of the four SG solutions. The adoption of full covariance matrices allows the correlations among the observed parameters to be entirely accounted for. As illustrated in Section *Data Editing*, the formal errors of the SG inputs reported in the covariance matrices of the SINEX files are overly optimistic. The optimal set of scaling factors to apply to the stated uncertainties of the SG inputs has been iteratively determined by executing KALREF-combination tests with the a posteriori variance factors obtained from the individual stacks illustrated in Table 3. Our tests led to estimates of the variance factors of $(3.07)^2$ for GNSS, $(2.98)^2$ for VLBI, $(2.61)^2$ for SLR, and $(1.36)^2$ for DORIS to be applied to the measurement covariance matrices during the data assimilation.

Frame Definition

To define origin and scale, the Helmert transformation parameters T_L, λ_L, λ_R in the rank-deficient system of Equations 4 are set to zero during the measurement update.

The condition $T_L = 0$ ensures translations are not estimated for SLR at each step of the measurement update, thus entailing the origin of the SLR network is not going to be adjusted. Since translations for the remaining SG techniques are not set to zero, the origin of VLBI, GNSS and DORIS networks are conversely being adjusted to SLR's quasi instantaneous origin (CM).

The conditions $\lambda_L = 0$, $\lambda_R = 0$ ensure that the SLR and VLBI scales are not adjusted during the weekly measurement updates. Scale parameters are estimated only for GNSS and DORIS, thus implying their intrinsic scale information is removed and adjusted to the weighted average scale defined by VLBI and SLR. Such definition will realize a combined TRF whose scale is given by the quasi instantaneous average of the interferometric (VLBI) and optical (SLR) scales weighted through the inverse of the covariance measurement matrices. Such an approach to the scale definition would be optimal were there no biases between VLBI and SLR-derived scales. Systematic scale and scale rate differences between the two observing systems, if existing, would not properly be reflected by the formal covariance matrices of the SG inputs. In recognizing this potential shortcoming, ITRF2014 adopted a scale definition based upon a simple average of the two systems, after having found a scale offset of 8.7 ± 0.6 mm at the epoch 2010.0 and a scale rate of 0.1 ± 0.1 mm/yr [3].

One way to assess potential scale and scale rate biases between VLBI and SLR in KALREF is to perform combination tests in which only λ_R is set to 0 in the system of Equations 4. Such an assumption entails adjusting SLR to VLBI scale at each step of the filter/smoother. The resulting time series of λ_L parameters therefore represents the time-varying scale offset between the two observing systems. Least squares fits of a linear regression model conducted on such scale offset time series can therefore provide an indication of the VLBI-to-SLR scale and scale rate bias. Assimilation tests executed by combining VLBI, SLR, DORIS, and GNSS inputs restricted to the IGS global network with a subset of 140 tie vectors whose covariance matrices have been scaled adopting the same set of variance factors selected for the JTRF2014 combination led to estimates of the VLBI-to-SLR scale offsets of -4.58 ± 0.10 to -4.93 ± 0.10 mm at January 1 2005, with scale rate differences of -0.22 ± 0.01 to -0.24 ± 0.01 mm/yr depending upon the station motion model chosen (simply linear or linear plus seasonal oscillators). Though suggestive of the existence of a scale bias, KALREF-derived estimates of the VLBI-to-SLR scale offsets turn out to be consistently smaller than the ones found in ITRF realizations [see e.g. 2, 3]. This evidence led

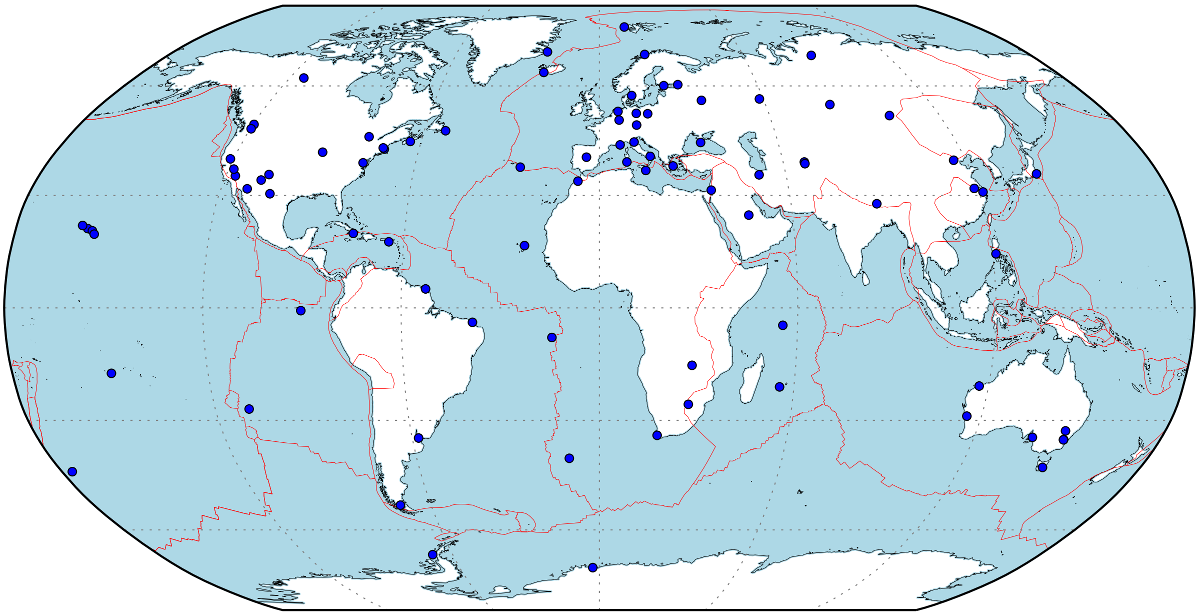

Fig. 2: *Spatial distribution of the 86 SG stations adopted for the application of the NNR conditions allowing JTRF2014 to be rotationally aligned to ITRF2008. Such reference sites are all characterized by long observing histories (larger than 10 years) and affected by less than 3 station position discontinuities.*

us to adopt the scale definition based upon the instantaneous weighted average of the SLR and VLBI scales. Further investigations are currently ongoing for a more in-depth analysis of the VLBI/SLR scale offsets in the context of Kalman Filter-based TRF combinations.

To define orientation, rotation parameters $(\mathbf{R_P}, \mathbf{R_R}, \mathbf{R_L}, \mathbf{R_D})$ featured in Equation 4 have been estimated for all of the 4 SG techniques and rotational minimal constraints to a subset of 86 stations (cf Figure 2) whose coordinates are expressed in the ITRF2008 have been applied at each step of the measurement update [cf Eq (4) in 38].

The reference sites represented in Figure 2 are characterized by long observing history (> 10 years) and affected by less than 3 station position discontinuities throughout their tracking history.

Co-motion Constraints

Adopting the state-space model illustrated in the Section *Kinematic Model and Time Update* and the coordinate the *total* displacement of the generic station i from the epoch k to $k+1$ can be described as

$$\tilde{x}^{ij}_{k+1} - \tilde{x}^{ij}_{k} = v^{ij}_{k} \cdot \Delta t + s^{ij}_{k+1} - s^{ij}_{k} + q^{ij}_{k+1} - q^{ij}_{k} + \varepsilon^{ij}_{x_k} \quad j = 1,2,3 \quad (6)$$

Co-motion constraints dictate the equivalence of the displacements of Equation 6 when observed by 2 or more nearby co-located stations, and require

- The trend variable (velocity) of co-located SG stations l and m be equivalent
- The seasonal oscillator state parameters relevant to co-located stations be the same.
- The station position process noise $\varepsilon_{x_k}^{lj}$ and $\varepsilon_{x_k}^{mj}$ relevant to co-located stations l and m be characterized by a 1.0 correlation coefficient.

The equivalence of the station velocities and of the seasonal oscillators for 2 generic co-located stations l and m is formalized through soft (stochastic) constraints associated with pre-assigned uncertainty:

$$\begin{cases} v_k^{lj} - v_k^{mj} = 0\,,\ (\sigma_v) \\ s_k^{lj} - s_k^{mj} = 0\,,\ (\sigma_s) \\ q_k^{lj} - q_k^{mj} = 0\,,\ (\sigma_q) \end{cases} \tag{7}$$

The constraints of Equations 7 provide additional measurement equations to be applied during the measurement update: velocity constraints in the first line of system of Equations 7 are applied at the first $(k = 1)$ step of the measurement update and, occasionally, at time steps immediately following velocity breaks; the seasonal constraints in the second (annual term) and third (semi-annual term) line are applied twice, at the first $(k = 1)$ and sixth $(k = 6)$ step of the measurement update.

The seasonal oscillator terms (cf Equation 2) for co-located stations are constrained to be equivalent with uncertainty value $\sigma_{s,q}$ uniformly set to $10\ \mu m$, based on the assumption that, conceivably, nearby stations are subject to and detect the same seasonal displacements. As to the velocity of co-moving stations, the uncertainties σ_v associated with the equivalence constraints are, unlike what happens for the seasonal oscillators, station-dependent. The exercise of establishing the most appropriate set of σ_v is a delicate one because of the impact it may have on temporal behavior of the frame-defining Helmert transformation parameters. In JTRF2014, velocity constraint-related uncertainties have been, once again, empirically determined by analyzing the time series of station position residuals at co-located sites, based on the assumption that inaccurately constrained velocities tend to produce systematically biased (non-zero mean) residual position time series. Default values for the velocity constraints are initially set to $1.0\ \mu m/yr$ for all of the co-locations with the exception of DORIS for which the uncertainties are loosened up to the level of $1.0\ mm/yr$. Based on the analysis of the position residuals, σ_v can be augmented and made, in exceptional cases, as high as $1.0\ cm/yr$.

The constraints on the station position processes $\varepsilon_{x_k}^{lj}$ and $\varepsilon_{x_k}^{mj}$ are realized by imposing the correlation term ρ_{lm} between stations l and m to be 1.0 in the process noise covariance matrix at each step of the forward filter.

Loading Models

UniLu-GGFC loading models describe the Earth elastic response to spatio-temporal mass variations in terrestrial fluid layers. The fluid-induced elastic displacements include contributions due to variation in continental water storage, atmospheric and ocean bottom pressure (OBP) and have been determined by convolving global geophysical fluid data with mass loading Green's functions [36] and load Love numbers as determined by [14].

The displacements caused by each fluid component have been computed separately at the sampling rate of the data and expressed through appropriate choice of the degree-1 load Love numbers in a CM-centered frame. The atmospheric loading displacements, supplied at 6 hourly intervals, have been derived from National Center for Environmental Prediction (NCEP) surface pressure fields making the assumption that the oceans behave like a modified inverted barometer. The Global Land Data Assimilation System (GLDAS/Noah) [28] has been used to compute 3 hourly time series of continental water storage-induced displacements. The ocean loading displacement time series are derived at 12 hourly intervals from JPL's Estimating the Circulation and Climate of the Ocean (ECCO) [12].

Despite the growing number of loading models with ever-increasing complexity in terms of geophysical fluid modelling, their direct adoption in SG reductions still poses relevant issues as to the contamination of the error models with the geodetic observations [24]. In JTRF2014, UniLu-GGFC data have been exclusively used to determine the station-dependent variance of the position process noise which represents the non-secular and non-seasonal deviation from the model of Equation 6.

The 3 fluid components of the displacements have been separately de-trended, de-seasonalized and subsequently aggregated in weekly averages. The residuals from each separate fluid component have been added up and first differences of the weekly global displacements have been computed. The variances of the differenced time series at each JTRF2014 site characterize the site-dependent position process noise $\varepsilon_{x_k}^{ij}$ of Equation 6. Median values of the square root of the the position process noise variances are found to be 1.20, 0.97, 2.22 mm with associated standard deviations of 0.10, 0.13, 0.87 mm for the North, East and Height component, respectively. Although the loading models do not account for either cryospheric (e.g. ice mass loss) or seismic processes, we found that the UniLu-GGFC-derived variances are large enough to allow for an adequate representation of some of the rapidly varying, non-linear and non-seasonal geophysical signals in the position time series.

JTRF2014 Main Results

By fully exploiting the sequential nature of the Kalman filter and RTS smoother algorithm, KALREF realizes time series-based TRFs at a sub-secular resolution giving access to the quasi instantaneous SLR-derived CM and to the quasi instantaneous scale realized by VLBI and SLR.

Station Position Time Series

JTRF2014 consists of a set of position time series of 972 stations at weekly intervals and daily combined EOPs along with their full covariance matrices. Station velocities may be used to produce, along with the seasonal oscillators, position predictions after 2015. To provide an indication of the internal precision of KALREF-derived station positions, an intrinsic stack of JTRF2014 SINEX files has been executed and time-dependent WRMS computed (cf Figure 3). The larger values of the WRMS in the time span 1980–1993 mostly reflect the poorer quality of the very early VLBI and SLR observations. As expected, WRMS tend to decrease as the data quality improves over time and, particularly, when GNSS observations start in the early 1990s.

An example of the station position time series outputted by KALREF is given in Figure 4 which illustrates the co-located GNSS and VLBI stations at Tsukuba (Japan). The black dots in the plots represent the observed positions of the two stations whereas the red solid lines indicate KALREF-estimated positions derived from JTRF2014. The co-seismic displacement of the two observing stations during the 9.1 Mw Tōhoku megaquake of March 11, 2011 is readily apparent, particularly in the East (see top panels of Figure 4) and Height (bottom panels) components. By resetting the variance of the station position process noise to 25.0 m^2 at the epoch of the seismic event, KALREF is able to correctly represent the sizable co-seismic dislocation. For TSKB, the GNSS station at Tsukuba, KALREF estimated a co-seismic displacement of 0.6153, 0.0341 and -0.0900 m in the East, North and Height component, respectively. In between discontinuities, the nominal value of the process noise at this site causes the KALREF-estimated station position to be a smoothed version of the observed position. The dynamical model of Equation 2 is used to interpolate across gaps in the observations and to extrapolate the station position to epochs before the station itself started observing (before 1994.0) or after it stopped observing (not shown in the plot). Since the VLBI station (7345) at Tsukuba is co-located with a GNSS station that started observing before it and because of the co-motion constraints applied to co-located stations, the KALREF-estimated position of the GNSS station is transferred to the VLBI station at the epochs in which 7345 was not yet operating. This is most clearly seen in the Height component (right bottom panel of Figure 4) in the time window 1994-1998.

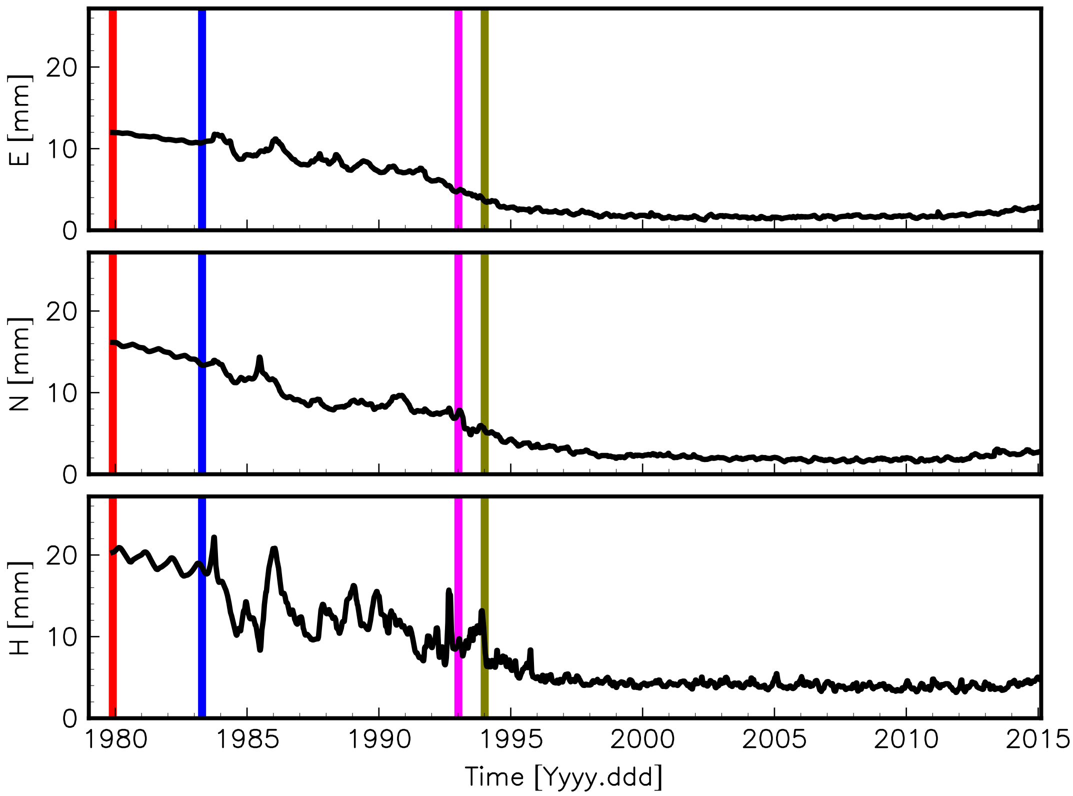

Fig. 3: *Temporal variability of the WRMS in the ENU space for KALREF-determined station position time series. WRMS are functions of the post-fit residuals of an intrinsic stack of JTRF2014 SINEX files. Sites exhibiting post-seismic relaxation effects have been removed from the JTRF2014 SINEX files prior to stacking. The solid red vertical line marks the epoch at which VLBI started observing. The solid blue line marks the epoch at which SLR started observing. The solid magenta and green lines mark the epochs at which DORIS and GNSS started observing.*

Local Ties and Agreement Between Ties and Space Geodesy

Local tie observations contain terrestrial estimates of SG reference points at co-location sites. During the measurement update, KALREF assimilates tie vectors providing linear constraints in the form of $X_i^C - X_j^C = \Delta\tilde{X}_{ij}$, where X_i^C and X_j^C are the station positions as determined through space-geodesy and $\Delta\tilde{X}_{ij}$ are 2017 the terrestrial tie measurements. Tie vectors are applied only once at the epoch of their measurement. Each of the tie constraints is weighted through the inverse of the measurement covariance matrices scaled by proper

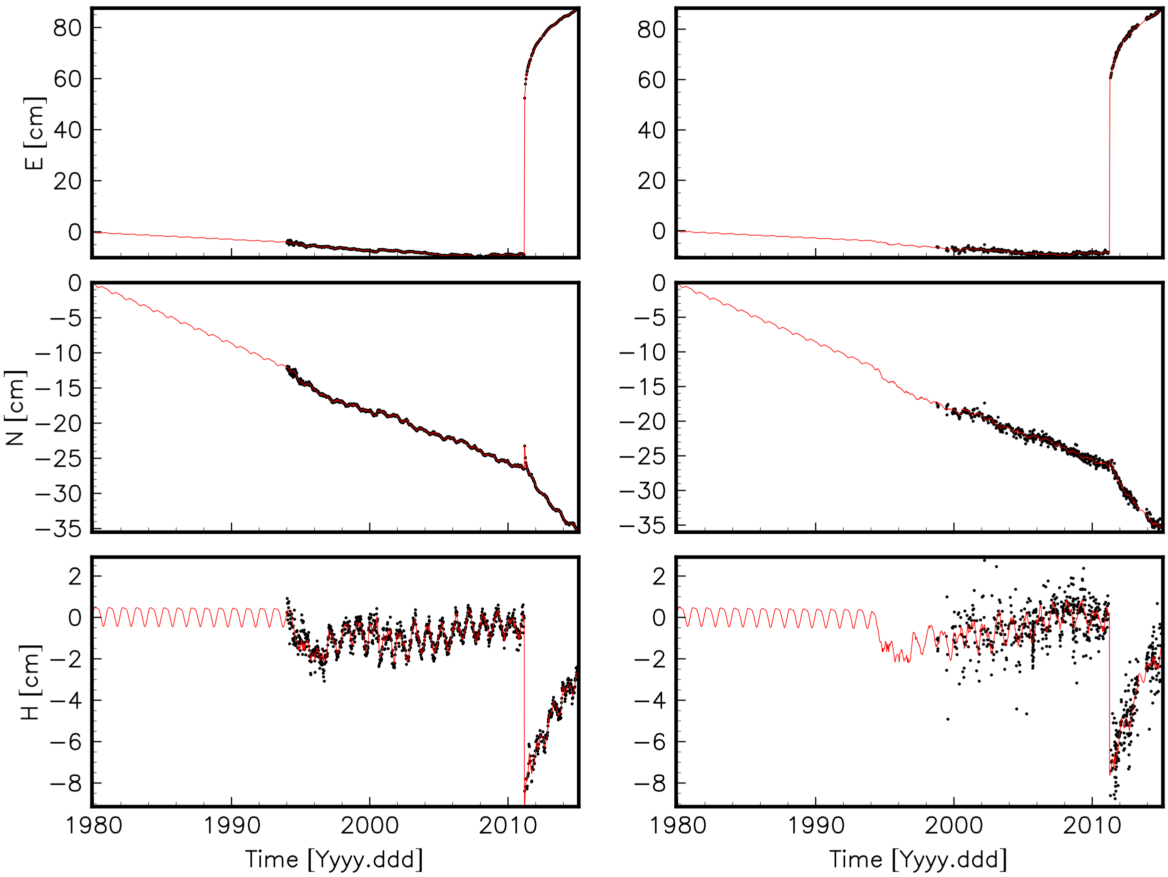

Fig. 4: *Position Time series for the co-located GNSS and VLBI stations at Tsukuba (Japan). The plots in the left panel relate to the GNSS station, whereas those on the right side to VLBI. Black dotted lines represent the station position observations assimilated by KALREF, the red solid lines are the weekly smoothed coordinates obtained as a result of the combination.*

variance factors. In JTRF2014 the optimal set of tie variance factors has been empirically determined as a function of the agreement between SG and terrestrial observations.

Post-fit tie residuals illustrate the agreement between terrestrial tie vector and SG observations. Ideally, in the absence of tie-related biases, the discrepancies between SG and terrestrial tie observations would provide a valuable proxy for assessing the internal accuracy of the SG techniques adopted in the assimilation. In reality, tie- and SG-related biases co-exist thus hindering the interpretation of tie residuals. In order to limit frame distortions in current frame reduction procedures, local ties, rather than SG observations, are down-weighted.

In JTRF2014, we adopted 234 tie vectors extracted from the total set of 142 site tie SINEX files made available by IGN-LAREG. Appendix 1, enclosed at the end of this document, lists the discrepancies for each of the tie vectors computed as differences (SG-Ties).

The results in Table 5 characterize the distribution of the tie residuals constituted by a set of 195 inter-technique terrestrial tie vectors connecting GNSS to the other SG systems. Tie residuals are classified by component in the local ENU space and by SG technique. A larger dispersion is observed in the vertical component of the residuals, with their inter-quartile variation being two to three times larger than the one of the horizontal components. The increased dispersion in the vertical component is suggestive of a poorer consistency (and therefore of a lesser accuracy) among the SG techniques in measuring the Earth radial deformations. Nonetheless tie-related biases affecting to a larger extent the vertical rather than the horizontal component cannot be ruled out. Technique-wise, it is worth observing that the IQR is consistently larger for tie vectors connecting GNSS to DORIS.

Geocenter Motion

Local tie observations and co-motion constraints have been used to connect the four SG techniques and, ultimately, to spatially and temporally transfer the SLR instantaneous CM information to the observing systems for which the geocenter is either poorly defined (such as GNSS and DORIS) or, which are, as is the case for VLBI, insensitive to GM (the product between the gravitational constant and Earth's mass). Properly tied to the SLR-derived CM-centered frame, the unified time series of KALREF-derived station positions from GNSS, DORIS and VLBI can therefore be adopted, in addition to SLR, to estimate Center of Mass to center of Network (CM-CN) offsets.

The JTRF2014-derived geocenter is based upon a selection of 80 stations extending the original ILRS network. Through the adoption of observing systems (GNSS, DORIS and VLBI) linked as a result of the combination to the SLR-derived CM, the ILRS network has been enlarged so as to include 66 stations in the Northern hemisphere and 14 in the

Table 5: *Statistical properties of the distribution of the site tie residuals computed as differences (SG-Ties) between combined space-geodetic and terrestrial tie observations. Statistics are expressed in mm in the ENU space, classified by SG techniques. Only site ties involving connections to GNSS have been considered when computing the values reported in this table. Same naming conventions for the SG techniques apply here (P is GNSS, R is VLBI, L is SLR, D is DORIS). st dev stands for standard deviation, IQR is the inter-quartile range, computed as the difference between the third and first quartile of the residual distribution.*

	N			E			H		
	R-P	L-P	D-P	R-P	L-P	D-P	R-P	L-P	D-P
min	-18.2	-25.2	-26.6	-52.5	-22.0	-35.4	-34.1	-42.4	-109.8
max	39.2	19.0	22.7	16.8	11.1	30.1	98.3	71.1	54.2
median	0.2	0.5	2.5	0.3	-0.4	-1.1	2.8	0.9	-2.2
st dev	10.2	7.2	9.2	10.4	6.6	10.0	20.6	20.7	22.2
IQR	5.0	6.8	11.0	6.0	6.2	11.4	13.8	18.7	20.2

Southern one. Although such configuration is still far from ideal for monitoring the temporal variations of (CM-CN), it is characterized by a better geographical coverage and, as a result of the spatio-temporal interpolations KALREF executes, unaffected by the large temporal turnover of the ILRS network.

The (CM-CN) offsets have been determined by applying the network shift approach [see e.g. 15] to the smoothed time series of station positions outputted by KALREF. The stacking model of Equation 1 has been adopted where the inverse of the measurement full covariance matrices has been used to weight the observations and only translations have been estimated. Internal translational constraints have been applied during the reduction in such a way that the resulting time series shown in Figure 5 are de-meaned and de-trended.

The gray-shaded area in Figure 5 identifies the time span during which only VLBI observations were being assimilated and SLR ranges were not available yet. In this time window, KALREF is backward extrapolating the geocenter information. The orange-shaded area marks the time window during which SLR stations were exclusively tracking LAGEOS 1. The first decade of SLR observations is characterized by large fluctuations of the (CM-CN) offsets which are likely to reflect the poorer data quality. When SLR ranges to LAGEOS 2, Etalon-1 and Etalon-2 were introduced starting from 1993, the quality of the geocenter (CM-CN) tends to improve and the large oscillations typical of the early years disappear. The power spectral density functions represented in the rightmost panels of Figure 5 show evidence of red-like behavior, with the power progressively decreasing as the frequency increases. With their temporal scatter (standard deviation) of 5.3, 4.9, and 10.9 mm on the T_x, T_y and T_z component respectively, the ILRS-derived geocenter motion time series appear much noisier than the ones determined from JTRF2014. Conversely, the JTRF2014-derived (CM-CN) time series are much smoother with standard deviations of 2.3, 3.0 and 4.8 mm for the T_x, T_y and T_z component, respectively and significantly reduced uncertainties. As a result of our combination approach, the combined station position time series from VLBI, GNSS, SLR and DORIS relate CM to a much larger and stable global SG network to the extent that the KALREF-derived (CM-CN) offsets are likely to better approximate the (CM-CF) motion.

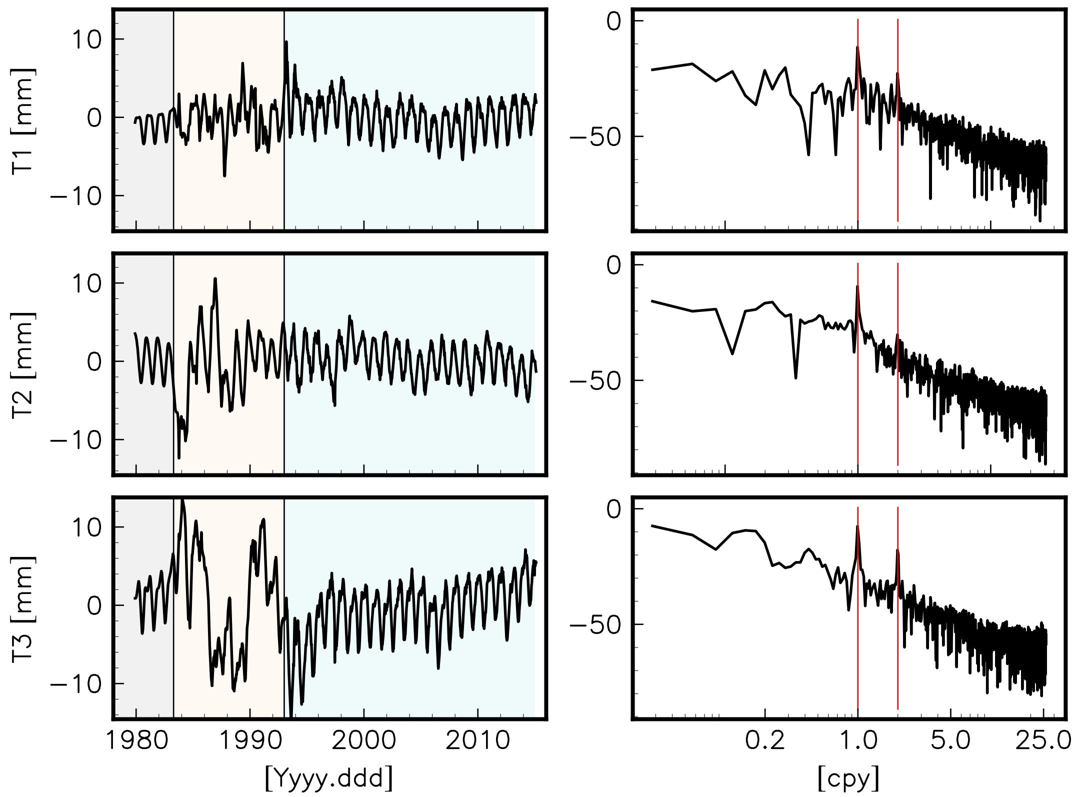

Fig. 5: *JTRF2014 geocenter Motion Time Series. Plots on the left side report the time series of the (CM-CN) offsets in mm. The time series WRMS about the mean are computed over the entire time span are 2.2, 2.3 and 3.5 mm for the x (T1), y (T2) and z (T3) components, respectively. The area shaded in gray identifies the time span 1979–1983 when only VLBI was observing and SLR data were not available yet. The orange-shaded area spans the time window 1983-1993 during which only LAGEOS 1 was being tracked and the ILRS solutions are based on fortnightly integrations. The area shaded in cyan spans the time window 1993–2015 during which the ILRS is a multi-satellite solution (LAGEOS 1 and 2 and Etalon 1 and 2 are being tracked) based on weekly integrations. Plots on the right side represent the time series in the spectral domain. Power spectral densities are expressed in dB mm^2/cpy, whereas frequencies are reported in cpy. Spectral lines at periods of 1 and 0.5 yr are marked in red.*

ITRF, JTRF and DTRF

In carrying out the mandate of providing ITRS realizations to the astronomical, geodetic and geophysical communities, the IERS acknowledges contributions from three accredited combination centres hosted by IGN-LAREG, JPL-Caltech, and DGFI-TUM. For the creation of the ITRF2014, three different frame products, consistently computed from the same input SINEX files released by the four SG Technique Centres were provided to IERS for evaluation purposes. The existence of three TRFs independently computed with different input data editing, handling of site ties, and combination schemes offers the possibility to soundly analyse the degree to which the three solutions agree with one another thus shedding light on systematic effects, differences evincing the diverse frame definitions, as well as the minute discrepancies that characterise the EOP series.

Table 6 documents and compares some of the essential features of the frame products maintained by IGN, JPL, and DGFI. In examining aspects related to the frame definition, it is worth observing that the three combination centres adhere to the standard practices described in Chapter 4 of [19] wherein a "frame definition chronology" for all the ITRS realizations, constructed by IGN-LAREG, from ITRF88 through ITRF2008 has also been outlined.

As to establishing the ITRS origin, we note that there have been isolated instances in the past in which both GPS and SLR simultaneously were taken to contribute to the geocentre defition. This practice has been long since dismissed for it has become apparent over the years that GNSS, despite its inherent sensitivity to Earth's GM, has proven deficient in recovering an unbiased CM-CN due to strong correlations between geodetic estimates of satellite clock offsets, station positions, and tropospheric parameters [26]. SLR therefore remains the golden standard for CM-CN determination and origin definition in TRF reductions, as evinced by Table 6.

The frame orientation is, unlike the origin, purely conventional and lately defined by *inheritance*, i.e. by applying analytical constraints that enforce the absence of residual rotations with respect to the most recent ITRS realizations (ITRF08 in the case of TRF2014 products, ITRF05 in the case of ITRF2008, and so forth). The frame scale, intimately related to the metric structure of the 3D Euclidean space, is – and has been in general – obtained by averaging radio-interferometric (VLBI) and optical (SLR) scales. Yet there have been instances in the relatively recent past (ITRF2005) in which the ITRF scale was only defined through VLBI, thus discarding the SLR contribution. Despite its sizeable dispersion (in the order of 10 mm about its mean value), VLBI scale evinces a larger stability as opposed to SLR's which appears to be affected by conspicuous time-variable biases [4].

According to the sets of conventional definitions reported in Chapter 4 of [19], the realization of a TRS relies on the notion of *regularized coordinates* in their relation to the instantaneous position of points (i.e. geodetic stations) anchored to Earth's crust:

$$X(t) \quad = \quad X^R(t) + \sum_i \Delta X_i(t). \tag{8}$$

The decomposition in Equation 8 dissects the instantaneous – and therefore time-variable – station position $X(t)$ into regularized coordinates $X^R(t)$ superimposed to high-frequency (mostly) tidal-related displacements $\Delta X_i(t)$; The former are directly provided by the frame realization, the latter are accessible through conventional geophysical models which are removed at the observation level within the SG reduction procedures.

Both TRS realizations from IGN and DGFI provide the users with regularized coordinates in *parameterized* form through monolithic SINEX files containing geocentric station positions expressed at a reference epoch, velocities, and EOPs along with their full covariance matrix.

In acknowledging the role that non-linear phenomena have on the time-varying deformable Earth and their impact on the frame quality, IGN chose to enhance, for the ITRF2014, its stacking model by adjusting periodic and post-seismic displacement (PSD) terms. Station harmonic motions and PSD for seismically active sites are themselves provided in parameterized form and can be utilized to construct more accurate station motion predictions. Due to the presence of PSD terms, the ITRF2014 station motion model is by far the most comprehensive among the three TRF products.

An opposing strategy for handling non-linearities is utilized by DGFI in DTRF2014. In analogy with standard processing of GRACE data where high-frequency non-tidal mass variability is removed from the range-rate observations and can be optionally restored by the users [11], DGFI applies a remove-restore approach to its frame reduction. Rather than fitting harmonic terms to position time series, DGFI removes from the SG coordinates geophysical models of non-tidal elastic displacements whose temporal and spatial sampling has been made consistent via spatial interpolation and numerical integration with SG data, and produces after-the-fact piecewise linear estimates of station positions. DTRF users, provided with the removed models, may optionally restore the non-tidal loading (NTL) variability into the frame product [32].

JPL-Caltech adopts a different approach to determining TRFs that relies on a Kalman filter and RTS smoother algorithm: JTRF users are provided with time series of quasi instantaneous geocentric position complying with the additive model outlined in Equation 6. Such geocentric time series consistently expressed in a common and rigorously defined frame, form long multi-technique SG records of the Earth's deformation, optimally assimilated and smoothed over the data time span of the combination (circa 1980–2015 for JTRF2014). As discussed in Section *Kinematic Model and Time update*, the station kinematic model accounts for trend terms and seasonal oscillators.

The adoption of process noise in the form of *random walk* imparts to JPL frame products a distinctive character. In allowing for deviations from the station motion model, the term ε_k in Equation 3 captures non-secular and non-seasonal components of the displacements thus enabling in principle a more realistic description of the time-variable nature of the deformable solid Earth.

To the extent that a random walk-based process noise is able to accurately represent the non-secular and non-seasonal components of the Earth deformation, JPL releases a frame product that turns out to be conceptually closer to a tide-free quasi instantaneous frame, rather than to a purely regularized product such as ITRF and DTRF (cf Equation 8). Moreover, JTRF being a sub-secular frame, its coordinates embed the quasi instantaneous variability due to smoothed SLR-sensed geocenter motion as well as the fluctuations of the quasi instantaneous VLBI/SLR scale. Users are therefore warned that a larger degree of variability is inherently present in JTRF, when compared to regularized and parameterized products such as ITRF and DTRF.

As mentioned in passing, when SG observations are no longer assimilable, KALREF may be run in predictive mode by adopting the propagator Φ_k in Equation 2 to project the state vector into the future without executing the measurement update. Unconstrained by SG data, KALREF forward filtering yields frame predictions that can be as usual outputted and delivered in form of SINEX files. Predictions are all of the more crucial in time series-based products such as JTRF in that they provide the only way to access the frame beyond its assimilation time span.

KALREF supports production of prediction SINEX files; However, these were not released for JTRF2014. Predictions are considered to be, at the current stage of development, experimental products still exhibiting deficiencies, particularly in relation to SG sites affected by post-seismic relaxation. Unlike ITRF, KALREF does not implement yet PSD terms in the state-space model of Equation 2. As a result, predictions for seismic sites are largely inaccurate and not adoptable in current SG reduction procedures. A further aspect, currently under investigation, relates to the selection of the most appropriate process noise capable of producing as accurate predictions as possible without degrading the temporal frame stability [35].

Unlike JTRF, ITRF and DTRF, both adopting a least square-based framework, do not allow for process noise in their frame reductions. In both products the stochastic component is rigorously accounted for only through the measurement covariance matrices (as reported in the input SINEX files) and propagated into the least square estimates and their uncertainties by means of standard covariance transformation laws.

ITRF products are computed with the software package CATREF built upon the framework of the *minimal constraint theory* [see e.g. 34]. CATREF, like KALREF, makes extensive use of the notion of similarity transformation whose constitutive elements are the Helmert transformation parameters. From the conceptual standpoint, similarities act on and between 3D Euclidean spaces by preserving their inherent geometrical structures (i.e. the *"shape"*). From the empirical standpoint, the Helmert transformation parameters can be conveniently adopted as metrics helping assess the degree to which two frames are reciprocally biased.

Unlike ITRF and JTRF, the DTRF approach to TRF analysis avoids the direct adoption of the similarity transformations and relies on the accumulation and combination of datum-free, rank-deficient Normal Equations constructed from the SG inputs [31]. Though not explicitly dependent upon the formulation of Helmert transformation parameters, DOGS also makes somewhat implicit use of a minimal constraint framework whenever *datum constraints* are either removed from or applied to the SG data [31].

Although the three combined products stem from identical input data sets, mutual discrepancies are expected for a variety of reasons involving, on the one hand, the different computational approaches and, on the other, the way in which systematic effects inherent in the observations are treated within the frame reductions. Both SG and local tie observations are known to be affected, to a various degree, by systematic effects not properly reflected in the measurement covariance matrices. Furthermore, relative weighting of the SG solutions and local tie observations, detection of position offsets, modelling of non-linear components of station motions, constitute additional factors potentially contributing to discrepancies in the three frame products.

The following Sections are entirely devoted to constructing metrics of frame consistency. To assess the extent to which the three frame solutions differ to one another, we performed inter-comparisons between JTRF2014, ITRF2014 and DTRF2014 based on (i) the determination of the time-variable offsets in terms of Helmert transformation parameters between the three frames determined in pairs with respect to ITRF2014 chosen as a reference and (ii) the analyses of the three different Earth Orientation series.

Helmert Transformation Parameters

The analysis of the time-variable offsets of the Helmert transformation parameters offers insights as to the way in which the three combined products have been constructed and lends itself particularly well to the definition of long-term consistency metrics (cf Table 7). The Helmert parameters described in this section provide least squares estimates of the linearized similarity transformation

$$X_i = X_{j,d} + T + \lambda X_{j,d} + \mathbf{R} X_{j,d} \tag{9}$$

where $X_{j,d}$ denotes either the JTRF2014 weekly position vector or the DTRF2014 station positions projected at the epoch t_k, X_i is the ITRF2014 station positions projected at the epoch t_k, T, λ and $\mathbf{R}$ are the translation vector, the scale factor and the antisymmetric rotation matrix mapping J(D)TRF2014 to ITRF2014 at the epoch t_k, respectively. The inverse of the covariance matrices reported in the TRF SINEX files has been adopted to weight the station position pseudo-observations from the three frames. Only ITRF2014 and DTRF2014 segments active at the epoch t_k have been considered in the least squares estimation problem. Active seismic sites have been removed from the frame products because, although ITRF2014 parameterizes post-seismic displacements and JTRF2014 tracks them thanks to station position process noise, DTRF2014 adopts piece-wise linear representation for stations characterised by post-seismic relaxation. In this analysis, time-dependent NTL corrections provided by DTRF2014 are not applied, because a rigorous covariance propagation of the models into the long-term frame is not feasible.

The time series shown in Figures 6 and 7 represent time-varying Helmerts mapping JTRF2014 to the projected ITRF2014 (right panels) and DTRF2014 (left panels). The first three plots from top of Figure 6 relate to the translations and point out the time-variable offset existing between the secular I(D)TRF2014 origins and the quasi instantaneous origin adopted by construction by JTRF2014. With the exception of Tx in the early years, the offsets to ITRF2014 and DTRF2014 evidence akin patterns and comparable temporal structures. The translation offsets in the X, Y and Z components exhibit, as expected, a seasonal signature mostly related to the sub-secular variation of the geocenter motion, unaccounted for in the I(D)TRF2014 combination process. If we were to restore time-dependent NTL corrections into DTRF2014, the translation offsets of Figure 6 would then represent discrepancies between JTRF2014 sub-secular geocenter motion and that implied by the non-tidal loading models adopted in the DTRF analyses. To the extent that such models provide a geophysically accurate representation of the degree-1 surface deformation signature, we expect translation offsets to diminish considerably when transforming JTRF2014 to DTRF2014+NTL.

Larger offset variations are observed in Tz and, to a lesser degree in Tx and Ty as well, during the time period 1984-1990, corresponding to the early years of the SLR observations, when only LAGEOS 1 was being tracked and, as a result of that, the (CM-CN) geocenter motion sensed by SLR was much noisier. After 1990, the origin differences appear much stabler over time.

The scale transformations to ITRF and DTRF also exhibit akin temporal variations with larger fluctuations in the early years which tend to subside after the introduction of LAGEOS-2 SLR observations in 1993. Afterwards, the λ's to both ITRF and DTRF exhibit a seasonal signature modulated with a quasi-decadal oscillation. It is worth observing, in this instance, that the estimates of the scale parameters through Equation 9 and their accurate interpretation are complicated by the existence of non-negligible mutual correlations among $(T, \lambda, \mathbf{R})$, possibly enhanced by the inhomogeneous distribution of the global SG networks.

Besides, Equation 9 is also prone to aliasing phenomena, mostly due to unwanted leakage of non-linear vertical station motion into the scale. This is particularly true when, as is the case with the transformation between the non-linear JTRF to the linear I(D)TRF, the assumption of similarity upon which Equation 9 is based is inherently violated. The polyhedrons X_i and X_d evolve linearly in time and are, in fact, not isomorphic to the non-linear Xj which, by virtue of the process noise, absorbs non-secular and non-seasonal motions. These two factors might partly explain the periodic signals present in the scale transformation, thus suggesting their artificial nature.

With WRMS about the linear trend smaller than 1 mm, the rotational Helmert parameters reported in Figure 7 exhibit the least fluctuations.

The estimates of offsets and drifts for each of the Helmert parameters gathered in Table 7 characterize the secular differences among the three frames and quantify their long-term agreement in terms of origin, scale, and rotational alignment. With the exception ot T_z and λ, the offsets are well within the 1 mm-level. We speculate the differences in T_z may be due to a different handling of local tie weighting within the JTRF–ITRF combinations.

More subtle to interpret is the scale parameter's behaviour. Since both JTRF and DTRF opted not to adjust VLBI's and SLR's scales in their combination schemes, their long-term scales appear to be, as evidenced by the values reported in Table 7, in larger agreement. Conversely, because ITRF2014 adjusted the SLR scale to an offset VLBI scale so as to account for the systematic difference between the two systems, the 1.7 mm offset at Jan 1 2005 in Table 7 mostly reflects the different scale definition adopted in ITRF2014 and JTRF2014.

Also, we observe that the time derivatives of the Helmert's mapping JTRF2014 to ITRF2014 are in the order of 0.18 mm/yr and even smaller for DTRF2014 (with the exception of $\dot{T}_z$ and $\dot{R}_y$). These results therefore indicate the level of long-term consistency between the three products is in the order of 0.18 mm/yr.

Table 6: *Synoptic outline of the combined products released by the official IERS ITRS Combination centres hosted at LAREG-IGN (ITRF), JPL-Caltech (JTRF), DGFI-TUM (DTRF). Additional pieces of information on the TRS-related activities promoted under the aegys of the IERS can be found on* https://www.iers.org/IERS/EN/Organization/ITRSCombinationCentres/ITRSCC.html*.*

	JTRF	**ITRF**	**DTRF**
Combination Center	JPL-Caltech	LAREG-IGN	DGFI-TUM
Computational Code	KALREF	CATREF	DOGS
Frame Type	Time Series	Parametric	Parametric
Estimator	Kalman Filter	Least-square	Least-square $^{(a)}$
Process Noise	Random Walk	None	None
Origin	Instantaneous SLR CM	Long-term SLR CM	Long-term SLR CM
Scale	Instantaneous VLBI/SLR	VLBI/SLR $^{(b)}$	VLBI/SLR $^{(c)}$
Orientation	NNR $^{(d)}$ to ITRF2008	NNR to ITRF2008	NNR to ITRF2008
Station Motion Model	Trend, Annual, Semi-Annual	Trend, Periodic, PSD $^{(e)}$	Trend, Non-Tidal Corrections

$^{(a)}$ Based on the inversion of accumulated Normal Equations

$^{(b)}$ Simple Average of VLBI and SLR Scales

$^{(c)}$ Weighted Average of VLBI and SLR Scales

$^{(d)}$ NNR stands for No-Net-Rotation

$^{(e)}$ PSD stands for Post-Seismic-Displacements

Earth Orientation Parameters

In all of three combined products, EOPs are adjusted conjointly with the global TRFs. Polar motion and polar motion rates therefore provide strong constraints ideally acting as inter-technique space-ties [see e.g. 22,23].

Considering the duality between frame rotational parameters and (x_p, y_p, UT) evidenced in Equation 5, the comparative analyses of the Earth Orientation series can be used to assess the degree of mutual consistency of ITRF, JTRF, and DTRF and to shed some light into the subtle differences characterizing the three products.

To verify the existence of systematisms affecting the three EOP series, in a first stage we form pair-wise differences to ITRF2014 restricting the analysis to the time span 1998–2015. In this exercise and in all the following analyses, prior to determining the differences, EOP interpolated values, purely based on a random walk model and unconstrained by actual measurements of the Earth rotational state, have been removed from the JPL series.

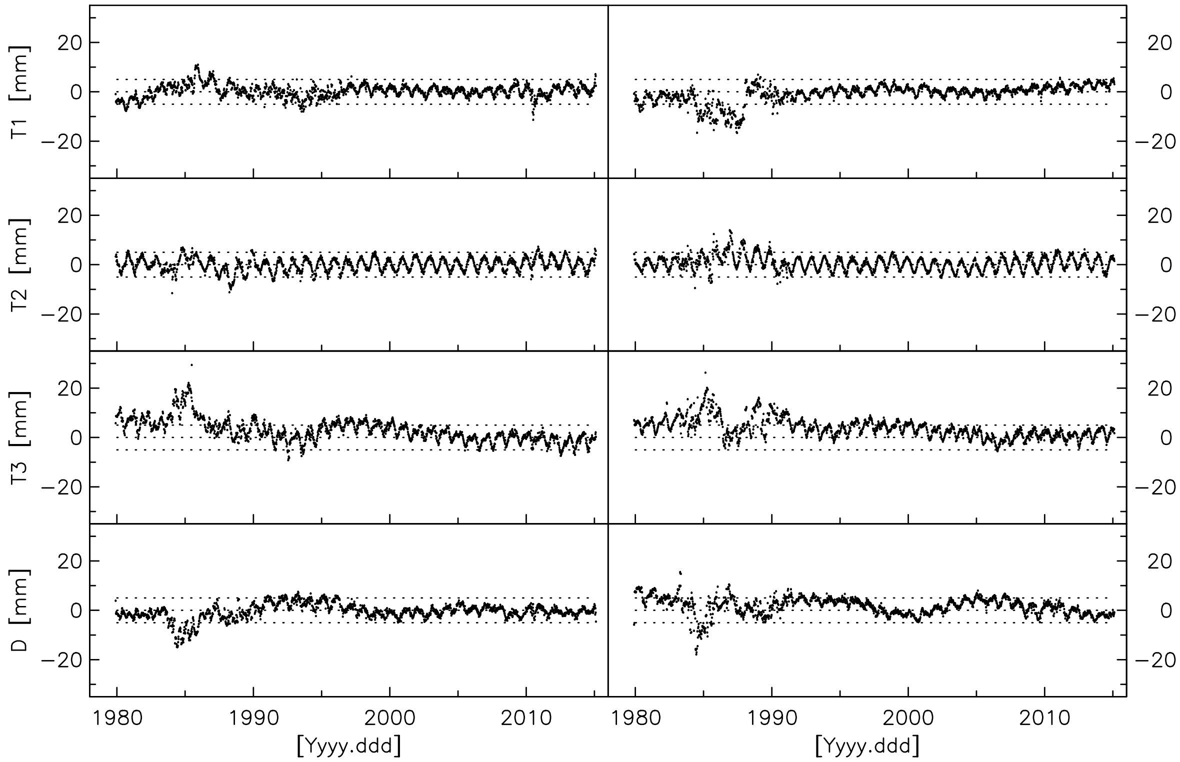

Fig. 6: *Time series of the Helmert Transformation parameters (translations and scale) from JTRF to ITRF/DTRF. Left panels illustrate Helmert offsets between JTRF and DTRF, whereas panels on the right are offsets between JTRF and ITRF. The dotted lines in all the panels represent the bounded region [-10,10]. Units are mm.*

As evidenced by the plots in Figure 8, the time series of the polar motion differences to ITRF2014 are both characterized by conspicuous residual signals in the form of linear trends and periodic signals at seasonal frequencies, whereas polar motion rates, UT and LOD differences are substantially flat.

We observe that, as can be seen from the least squares fits of Table 8, the linear trends of the pole coordinate differences are in the order of a few micro-arcseconds. With a value of 5.35 μas/day on YPO, the largest rate is found for the JTRF-to-ITRF differences. Likewise, the seasonal amplitudes of the XPO and YPO JTRF-to-ITRF differences are the highest.

To isolate the source of such perturbations, an independent Earth orientation series with signal-to-noise ratio comparable to the combined products would be needed. For this purpose, we adopt COMB2016,

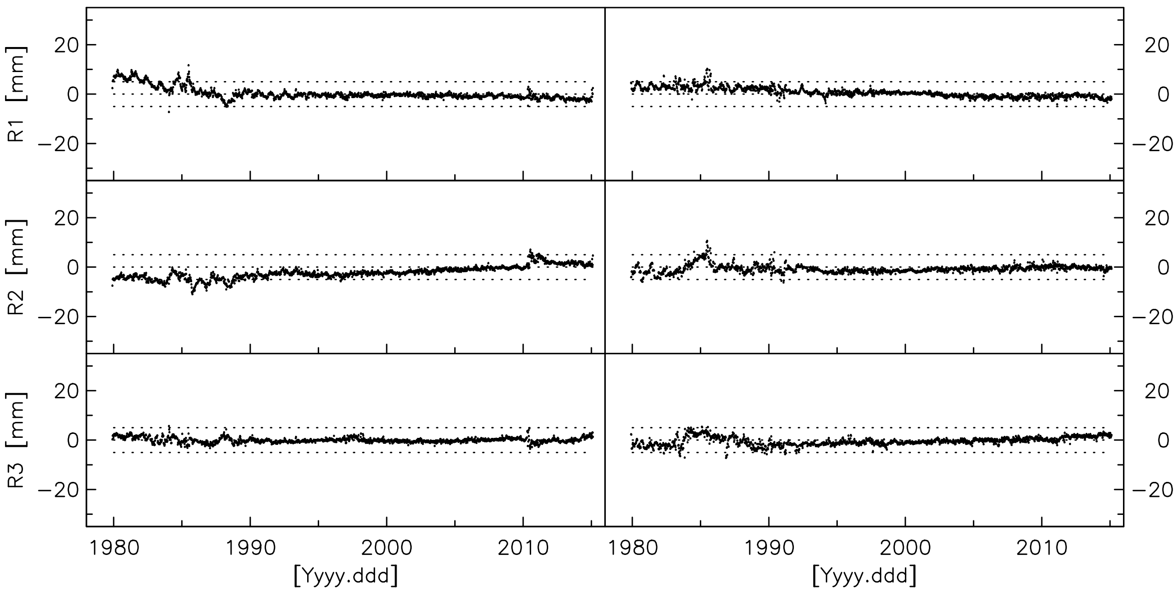

Fig. 7: *Time series of the Helmert Transformation parameters (rotations) from JTRF to ITRF/DTRF. Left panels illustrate Helmert offsets between JTRF and DTRF, whereas panels on the right are offsets between JTRF and ITRF. The dotted lines in all the panels represent the bounded region [-10,10]. Units are mm.*

the EOP series that JPL constructs with a Kalman filter approach by combining an ensemble of optical astrometry and SG observations based on LLR, SLR, VLBI, and GPS spanning the time window 1976–2017. EOP data are calibrated in isolation, i.e. inter-technique biases and rate biases are determined by disassociating the observations from their underlying TRFs [21].

Though not entirely independent of the inputs employed in TRF reductions, COMB makes additional use of astrometric and LLR data unaccounted for in IERS TRF combinations and suffers less from the adverse effects of multiple reference frame changes plaguing products such as the operational IGS polar motion series.

Moreover, COMB2016 series is rotationally consistent with ITRF2014 and is sampled and provided at daily intervals available at, unlike analogous products such as IERSC04 [6], either noon or midnight. This last feature is particularly appealing when comparisons to TRF-related products are needed since combined TRF EOPs are, unlike IERSC04, traditionally outputted at noon.

That COMB2016 is rotationally consistent with ITRF2014 can be deduced from the estimates of biases and rates to ITRF reported in Table 9, which are the least found. When compared to COMB2016, all of the three pole time series bear indication of corruption to a varying degree at seasonal frequencies (particularly at the annual). As far as XPO, the level of agreement of the annual signal of the three series to COMB is within the range 6–9 μas. At semi-annual periods, DTRF2014 differences appear to be characterised by larger amplitudes in the order of 9 μas. We found the differences JTRF2014 to COMB2016 polar motions are characterised by annual amplitudes markedly larger for YPO (cf Table 9). We speculate the residual seasonal signals in the JTRF2014 polar motion may result from the inconsistency between the daily resolution of the EOPs and the linear site motion approximation of the ITRF2008 adopted to define the orientation of the non-linear JTRF2014.

Likewise, it cannot be ruled out at this stage of the analysis that unwanted systematic perturbations to the EOP time series have been introduced both by IGN, when fitting seasonal terms during the single-technique stacks, and DGFI, during the removal of NTL corrections.

Incidentally, we observe that, when all of the systematic effects are removed, the dispersions of the residuals as quantified by the RMS are consistently smaller for JTRF. Yet the RMS differences are minute, often in the order of a few micro-arcseconds and therefore likely to be below noise level.

If we circle back to the plots of Figure 8, we notice that the UT dispersion is visibly larger for the DTRF differences to ITRF (cf also RMS in the Table 8). Likewise, the dispersion of polar motion rates and LOD residuals are found to be the largest for the DTRF differences to ITRF, with RMS values one order of magnitude larger than JTRF. We speculate the larger dispersions of UT and LOD from DTRF2014 may be due to a different handling of the input EOP data within the DTRF processing scheme: DGFI is the only combination center combining LOD observations from GNSS and SLR (see comparative Table 10). Indeed, the adoption of satellite-derived LOD in EOP combinations is still rather controversial: GNSS-derived LOD appears to be affected by time-varying biases which are only partially mitigated in the IGS reprocessing [27]. Likewise, ILRS-derived LOD, far from being constrained by a robust multi-satellite geometry as described in [8], may still suffer from sizeable correlations with orbital parameters such as the nodal precession rate.

To assess the uncertainty of the combined polar motion, UT and their rates, a three-corner hat (TCH) approach has been applied to the Earth

Orientation series from JPL, IGN, and DGFI. Only simultaneous measurements of the Earth rotational state common to the three series in the time window 1998–2015 have been used in this analysis. TCH has been applied by following the implementation outlined in [20] where the authors, in addition to computing the unknown process noise variance of each of the three time series, also solve for their mutual correlations. Additional constraints enforcing the positive definiteness of the covariance matrix of the unknowns have also been implemented.

TCH operates by forming pair-wise differences between time-based measurements of the same physical processes from three (or more) observing systems. Implicit in TCH is the idea that, when forming the processes of the differences, common-mode signals/errors are eliminated in such a way that the TCH-derived uncertainties allegedly represent the variance of the process noise associated with each of the series.

As evidenced by the results in Table 8, the time series of the EOP differences to ITRF2014 are both characterized by significant residual signals (trends and seasonals), none of which has been removed prior to forming differences. Hence the TCH results reported in Table 11 may be affected to some degree by the different character of the seasonal and linear trend terms described in Table 8.

With UT- and LOD-related uncertainties being much larger for DTRF than the other centres, the results of Table 11 corroborate the inferences about the adverse effects that the adoption of satellite-derived LOD observations has on UT in the DGFI combination. DTRF-derived polar motion rates are also characterized by uncertainties one order of magnitude larger than ITRF's and JTRF's.

With the only exception of UT, ITRF2014's EOPs, followed by JTRF2014's, turn out to be characterised by the smallest uncertainties. The YPO uncertainty for JTRF2014 is the highest found, and this is not surprising considering the fact that TCH is most likely to absorb part of the anomalously large seasonal variability affecting JPL's YPO (cf Table 8). Incidentally we observe that YPO from DTRF2014 appears to be the precisest in the TCH sense.

Though highly appealing for its straightforward analytical formulation, TCH relies on a set of assumptions which appear to be too restrictive when applied to potentially correlated sets of precise observations of the Earth rotational state.

The assumption of absence of correlation between the three classes of observations and their underlying process noise is barely acceptable, considering the fact that the three solutions stem from the same input data. The modified TCH approach here implemented tries to overcome such limitation by introducing mutual correlations as additional unknowns in the estimation problems. [20].

Even more critical is the presence of temporally correlated noise processes affecting to a various extent the EOP series which TCH is not able by design to account for. Tests have been conducted on simulated data sets in order to assess the impact of time-correlated noise, such as random walk, on TCH results. Our simulations show that as the random walk levels injected in the time series increase, TCH tends to overestimate the uncertainties and appears unable to correctly recover the true uncertainties.

A more sophisticated approach to assessing the intrinsic noise level associated with each of the three EOP products blends standard time- and frequency-domain techniques allowing for a more accurate representation of the frequency-dependent nature of the EOP process noise. By recognizing that low-order autoregressive (AR) processes are fit to approximate the background noise in EOP series, we estimate the AR-related parameters in the frequency domain and we adopt the AR-related white noise to quantify the noise level in each series. In the following, we show how such an approach can be easily applied to polar motion data.

That standard Fourier analyses of EOP parameters bear uncontrovertible evidence of processes wherein power is enhanced at lowest frequencies and monotonically decays as the frequency increase can be easily seen in Figure 10, where the retrograde/prograde amplitude spectrum (black solid line) of JTRF2014 polar motion is represented.

We observe that, although x_p and y_p have been both detrended before being Fourier transformed, the polar motion spectrum exhibits a considerably high dynamical range in the order of 10^3. To minimize spectral leakage and aliasing, the polar motion observations have been tapered with discrete prolate spherical sequences characterized by maximal energy concentration and the final amplitude spectrum has been determined through an adaptively weighted average of Slepian-tapered “eigenspectra“ as described in [18]. We made sure the time product bandwidth selected for the multi-tapering would not cause excessive spectral smoothing and, at the same time, allow for an adequate representation of the high dynamic range of the process.

To suppress peaks across all of the spectral frequencies, a median filter with moving window of semi-width of 0.004 cpd has been run on the spectrum (thick gray line in Figure 10). Once the peaks largely corresponding to signal of geophysical nature are removed, the median spectrum can be taken to represent the frequency-dependent background noise level associated with polar motion data.

The simplest description in the time domain of a discrete finite series characterized by red noise is a causal first-order autoregressive process – termed as AR(1) in the following:

$$x_n = \phi x_{n-1} + w_n \quad \phi \in]0, 1[\tag{10}$$

where the integer $n = 1, \ldots, N$ denotes the discrete time increments in units of the sampling interval Δt (day, in this case), the coefficient ϕ quantifies the degree of persistence between consecutive terms in the series, $w_n \sim \mathcal{N}(0, \sigma^2)$ is the n-th realization of a Gaussian process with zero-mean and variance σ^2. Positive values of ϕ are indicative of a spectrum wherein the power of low frequency components is enhanced, as is the case for polar motion and most geophysical processes. Negative values of ϕ conversely describe non-causal and explosive processes whose power spectrum is monotonically increasing with f and therefore enhanced at higher frequencies (the so-called blue noise). The power spectral density of an AR(1) process can be described as follows [see e.g. 33]:

$$S(f) = \frac{\sigma^2}{1 - 2\phi\cos(\frac{\pi f}{f_n}) + \phi^2} \tag{11}$$

where f and f_n denote the frequency and the Nyquist frequency, respectively. We observe that, when ϕ is positive and smaller than one, Equation 11 is representative of a power spectral density decaying to zero for increasing frequencies. When $\phi = 1$, the AR(1) degenerates to a random-walk and the power spectrum, theoretically undefined for non-stationary processes, is discontinuous at $f = 0$. When ϕ approaches zero, Equation 11 degenerates to a pure white noise spectrum.

The spectrum of Equation 11 is a non-linear function in the parameters (σ, ϕ), which can be estimated via Bayesian regression from a realization of the empirical spectrum (i.e. the thick gray line in Figure 10).

Uninformative (i.e. uniform) priors have been adopted on (σ, ϕ) with additional constraints enforcing the positivity of the variance factor and restricting ϕ to $]0, 1[$.

To the extent that the estimate of the AR(1) parameters leads to an accurate representation of the polar motion background noise level, then Equation 11 can be effectively used to define a frequency-dependent signal-to-noise ratio for polar motion. By inspecting Figure 10, we note that the AR(1) representation (red line) might underfit the high-frequency portion of the empirical spectrum (gray line).

Table 12 collects median values of the parameters drawn from the posterior distribution. With estimates of ϕ close to unity in all cases, the background noise process in EOP series appears to be consistent with random walk. Since σ quantifies the amount of white noise in the EOP series, it conveys an informative content analogous to the TCH uncertainties reported in Table 11, with the only difference that TCH has been run separately on the two equatorial components XPO and YPO, whereas the estimates of Table 12 are indicative of the complex polar motion signal $p(t) = x_p(t) - iy_p(t)$. The direct comparison of the results reported in Table 11 with those of Table 12 points out that AR(1)-related white noise estimates are on the whole smaller than TCH's, thus corroborating the hypothesis that TCH may overestimate the polar motion uncertainties. The spectral estimates of the white noise levels for the three EOP series are much closer to one another than TCH's. The largest differences being in the order of $\approx 3\ \mu as$, they are likely to be well below the noise level. Therefore the AR(1)-related estimates appear to suggest that the polar motion series are of comparable quality. Incidentally, we note that DTRF polar motion is, in the AR(1) sense, characterized by the lowest white noise level whereas COMB polar motion has the highest.

Some Final Considerations

JTRF2014 is a sub-secular TRF based on a Kalman filter and RTS smoother and obtained by combining SG inputs from VLBI, SLR, GNSS, and DORIS. The multi-technique position time series associated with JTRF2014 are accurately linked to the SLR CM frame through the usage of local ties and the implementation of co-motion constraints.

Though still far from representing a standard operational TRF product, JTRF offers to the geodetic and geophysical community tantalizing features. With its time series representation, JTRF gives access to a quasi-instantaneous CM as sensed by SLR as well as to a quasi-instantaneous scale as realized by VLBI and SLR which, if accurately realized by data, can be used by geodetic systems with inaccurate scale infomration for monitoring time-variable station coordinates.

The time-variable geocentric station coordinates appear to describe the Earth deformation reasonably well during tracking periods and short data gaps. The JTRF2014 unified time series have been used to infer temporal variations of (CM-CN) offsets which appear to be in good agreement with the quasi-independent geocenter motion estimated via spectral inversion of GNSS, GRACE and ECCO-derived OBP variations [37].

In an effort to modernize the computational code, improvements to KALREF are currently being tested. These relate to e.g. strategies for providing accurate predictions of the station motions, data-editing pipelines, break detection, the transition to a more flexible and numerically stabler square-root information filter with a time-variable step, the adoption of a dynamical model for daily EOPs.

As efforts to improve KALREF and to research time-series based TRFs continue, positive feedback on JTRF2014 has been received. When adopted in precise orbit determination of high and low Earth orbiters

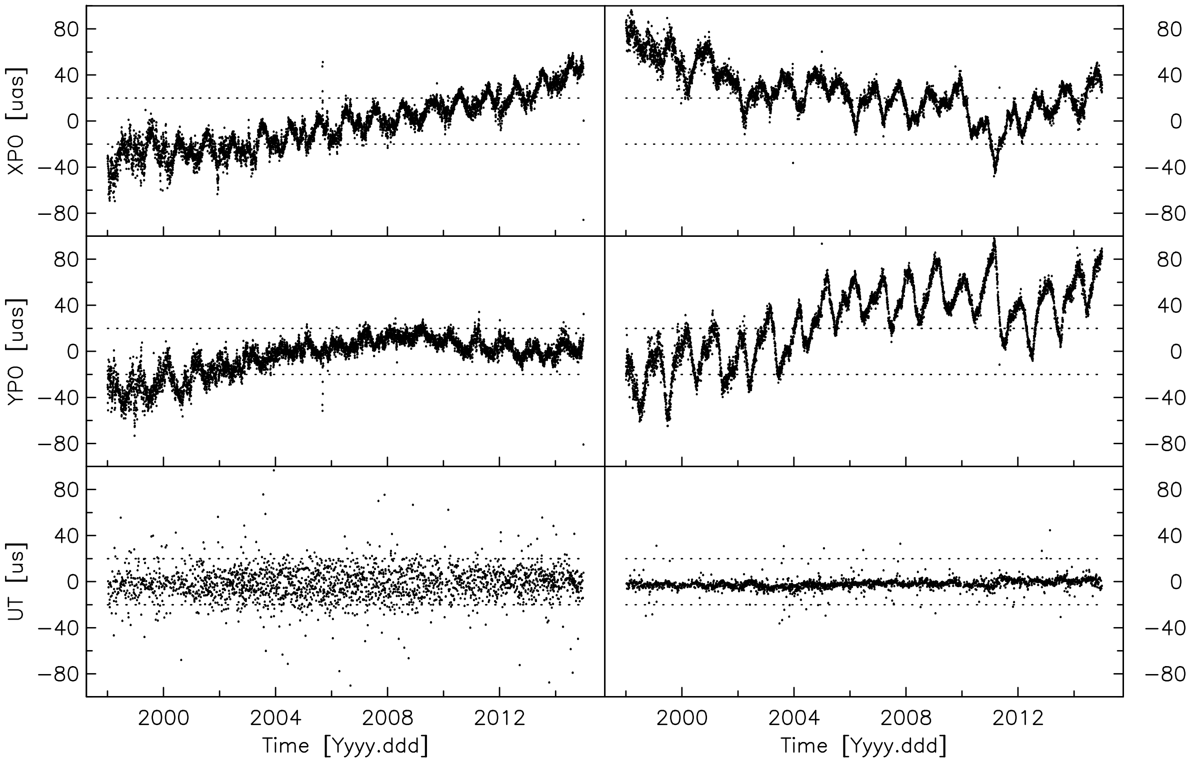

Fig. 8: *Time series of the polar motion differences to ITRF. Left panels illustrate differences (DTRF–ITRF), whereas panels on the right are differences (JTRF–ITRF). Dotted black lines in the plots mark the range* $[-20.0, 20.0]$*. Values of the EOP differences larger than* $|100.0|$ *have been filtered out. Units are* μas *for the pole coordinates* (x_p, y_p)*, and* $\mu sec/d$ *for* UT*.*

JTRF2014-derived time series are reported to make valuable contributions in terms of reduction of post-fit residuals and an improved geocenter determination [see e.g. 39, 29]

The inter-comparisons among ITRF, JTRF, and DTRF suggest a high level of long-term consistency of the three products: the offsets at January 1, 2005 of the Helmert transformation parameters relating JTRF2014 and DTRF2014 to ITRF2014 are in the order of 1 mm with the exception of the JTRF-to-ITRF scale, whose larger offset (1.70 mm) is attributable to the different strategy adopted in averaging the VLBI/SLR scale information. The scale offset mapping JTRF to DTRF is close to zero with no significant drift found.

In this regard, we wish to warn the readers not to misinterpret such a finding: The absence of scale offset and drift between the JPL and DGFI solution merely suggests that the two TRFs adopted a somewhat

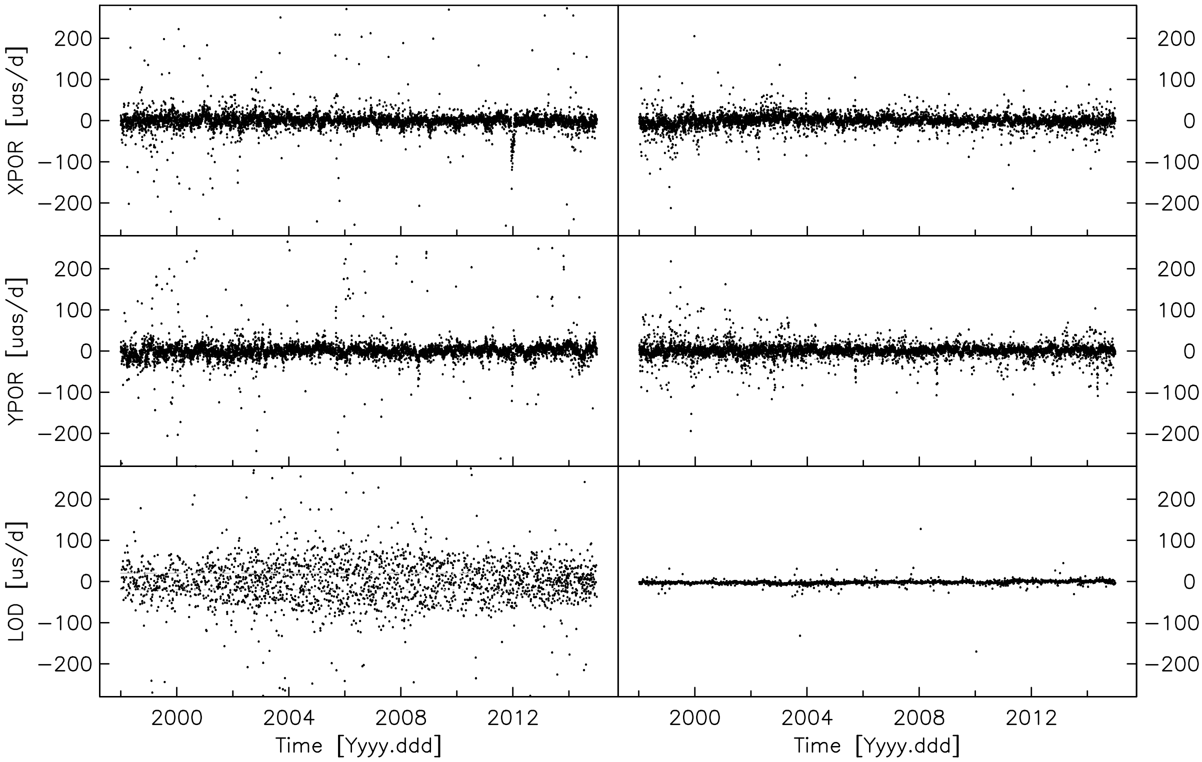

Fig. 9: *Time series of the polar motion rates differences to ITRF. Left panels illustrate differences (DTRF–ITRF), whereas panels on the right are differences (JTRF–ITRF). Units are* $\mu as/d$ *for the pole coordinates* $(\dot{x}_p, \dot{y}_p)$*, and* $\mu s/d$ *for* LOD*.*

akin scale definition, i.e. neither VLBI's nor SLR's scale have been adjusted during the combination. No inference can be made from the results presented in Table 7 as to the existence of a VLBI/SLR scale bias. The determination of the time variable nature of the VLBI/SLR scale bias requires special analyses of the IVS and ILRS input data sets tied through local ties, whose results were not reported in this note.

Drifts of the Helmert transformation parameters between ITRF and JTRF are found to be smaller than 0.18 mm/yr. The drifts between DTRF and JTRF are even smaller, with the exception of a large trend (-0.42 mm/yr) found on T_z.

It is important to stress that the results presented in Section *ITRF, JTRF, and DTRF* uniquely address reciprocal consistency of the three frame products. No inference can be made at this stage of the analysis regarding TRF accuracy (i.e. degree of closeness to some external "truth").

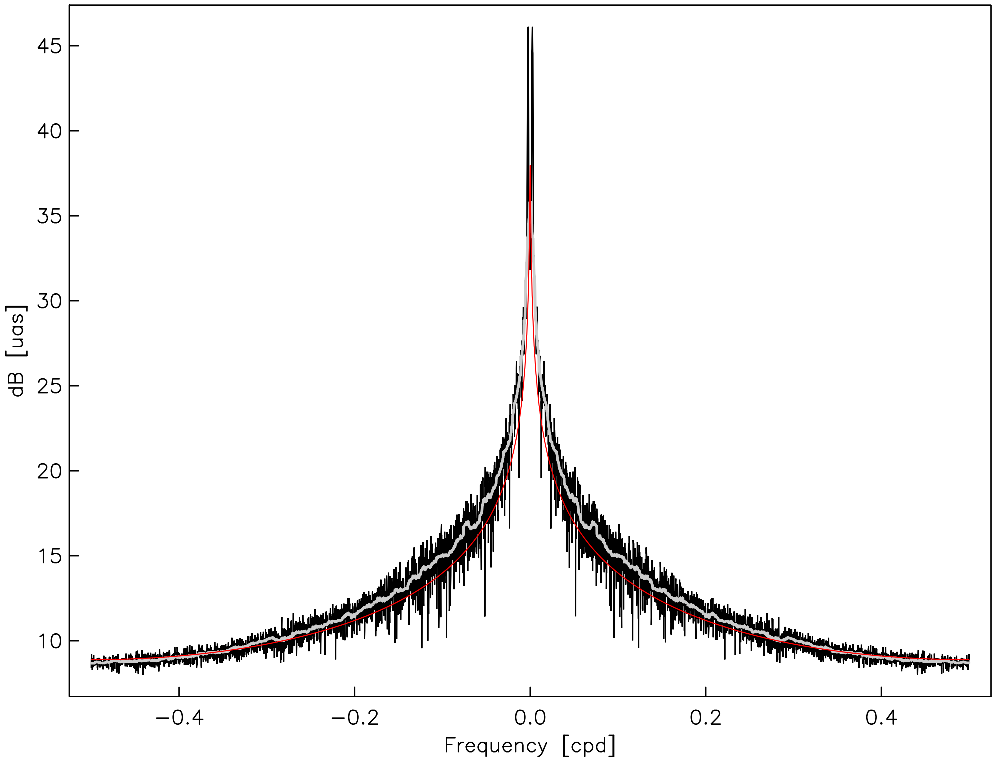

Fig. 10: *Amplitude Spectrum of the polar motion signal* $(x_p - iy_p)$ *from JTRF2014. The black solid curve represents the adaptively weighted amplitude spectrum determined via multitaper approach. The time-bandwidth product NW has been set to 3, and the corresponding (2NW-1) Slepian functions were used as tapers. The solid gray curve reports the median spectrum determined from the black line with a window of semi-width w set to 0.004 cpd.*

Users should be aware of the fact that JTRF station positions are characterized by much a larger variability than standard parameterized products because (i) KALREF adopts a station motion model based on trend and seasonal terms, (ii) JTRF coordinates reflect, unlike ITRF and DTRF, week-to-week geocentre as well as scale variability.

In future JTRF realizations, the quasi instantaneous scale representation can be improved by accounting for potential systematic effects between VLBI's and SLR's scales. Yet the adoption of such a scale may prove challenging: JTRF2014 pointed out larger oscillations of the scale parameters in the early years of the observations (before 1993.0). The nature of such oscillations (geophysical signal versus inherent noise of the observing systems) should be ascertained. If such oscillations prove unphysical because mostly due to larger noise of the two systems, then such noise may get directly transferred to the height component of the station motion. One way to alleviate this effect might come from adopting the scale information derived from independently calibrated GNSS observations [13]: KALREF could be made flexible enough to allow for a scale definition based on a VLBI/SLR secular scale superimposed with the day-to-day variabilily provided by the "dynamic" GNSS's scale.

As efforts to improve IERS-ITRF products are being made, it is mandatory that the Technique Centres pursue and foster in-depth analyses aimed at assessing technique-specific systematic effests.

ILRS is, as of this writing, testing the effect of the introduction in the data reduction of time-variable range biases at all SLR stations on the scale definition. Such an approach proved instrumental in partially reconciling SLR's to VLBI's scale [see e.g. 4].

IVS should consider assessing the effects of structural deformations in VLBI radiotelescope with particular regard to the scale parameter [30].

The scale remains the major source of inconsistencies in TRF products. From KALREF's standpoint, further investigations are required to assess (and to understand) the scale differences between VLBI and SLR under the various possible configurations offered by the computational code (e.g. the activation of process noise while determining the scale difference between VLBI and SLR appears to exacerbate the time-variable biases).

JTRF is a sub-secular and inherently non-linear frame, whereas DTRF and ITRF are primarily secular frames. The representation of non-linear phenomena in ITRF and DTRF is possible through the introduction of correction terms. ITRF2014 provides seasonal and PSD terms in parameterized form to account for non-linear behaviour. DTRF2014, which was computed by removing NTL displacements from the input SINEX files, supplies the NTL corrections for users interested in restoring the non tidal loading variability.

The analyses of EOP consistency pointed out that all of the three Earth rotation time series are affected to a varying degree by systematisms. We found evidence of statistically significant trend and seasonal terms in the EOP differences from ITRF, JTRF, and DTRF to COMB2016. This is particularly evident for polar motion observations. JTRF YPO is affected by an anomalously large annual component.

ITRF and DTRF also bear indication of significant EOP contaminations at the seasonal frequencies. When systematic effects are removed from the combined polar motion, the RMS of the differences (JTRF–ITRF) and (DTRF–ITRF) are in the order of 10 μas.

TCH results applied to polar motion time series in the time interval 1998–2015 suggest the uncertainties are well within the range [15,30] μas. Polar motion rates from DTRF are affected by larger dispersion, when compared to ITRF and DTRF. TCH applied to the three time series confirm a clear degradation of LOD and UT for DTRF. Yet there are indications that TCH results may be affected by time-correlated errors inherent to the EOP series.

Time- and spectral-domain approaches applied to the polar motion series suggests that TCH may overestimate the square root of the process noise variance up to a factor two. Estimation of the noise content based on a simple AR(1) model seems to suggest that the σ associated with white noise in polar motion series ranges within [12,16] μas, thus testifying the excellent level of consistency between the three products.

Acknowledgements

This work was carried out at the Jet Propulsion Laboratory, California Institute of Technology, under a contract with the National Aeronautics and Space Administration (NASA). We gratefully acknowledge funding support from NASA's Space Geodesy Program.

B Soja's research was supported by an appointment to the NASA Postdoctoral Program at the NASA Jet Propulsion Laboratory, administered by Universities Space Research Association under contract with NASA.

The valuable contributions from the Space-Geodetic Technique Services (IVS, ILRS, IGS and IDS) continuously providing data for the IERS-ITRF combination projects are acknowledged.

JTRF2014 SINEX files as well as associated files such as station position time series, Earth Orientation series, geocenter motion (CM-CN) time series are available upon request (claudio.abbondanza@jpl.nasa.gov).

Maps in this manuscript have been produced with CartoPy, freely available under the terms of the GNU License.

U.S. Government sponsorship acknowledged.

Table 7: *Linear regression of the time series of the Helmert transformation parameters mapping JTRF2014 to ITRF2014 and DTRF2014 represented in Figures 6 and 7. Values in the Table are determined via least-square estimation of the model* $h(t) = a + b \cdot (t - t_0)$ *applied to the time series of Figures 6 and 7 restricted to the time span 1995–2015. The row (a) reports the offset estimates whereas (b) the time derivatives of the transformation parameters. Offsets and trends are converted into surface equivalent displacements and rates of surface equivalent displacements and suitably expressed in mm at the reference epoch* t_0 *Jan 1 2005 and in* mm/yr*, respectively. Parenthesized are* $(1 \cdot \sigma)$ *formal errors.*

		T_1	T_2	T_3	λ	R_1	R_2	R_3
JTRF to ITRF	(a)	0.40 (0.04)	-0.21 (0.04)	1.45 (0.05)	1.70 (0.08)	-0.69 (0.02)	-0.81 (0.02)	-0.22 (0.02)
	(b)	0.17 (0.01)	0.12 (0.01)	-0.18 (0.01)	-0.18 (0.01)	-0.11 (0.01)	0.10 (0.00)	0.16 (0.01)
JTRF to DTRF	(a)	0.37 (0.04)	0.11 (0.03)	1.10 (0.04)	-0.27 (0.04)	-0.76 (0.02)	-1.03 (0.02)	-0.23 (0.02)
	(b)	-0.05 (0.01)	0.02 (0.01)	-0.42 (0.01)	-0.02 (0.01)	-0.07 (0.01)	0.29 (0.01)	-0.01 (0.01)

Table 8: *Least-square fits of the EOP differences to ITRF to the model* $h(t) = a+b\cdot(t-t_0)+c\cdot\sin\left[\omega(t-t_0)-\varphi\right]$*, where* h *is the generic Earth Orientation parameter,* a *is the bias,* b *is the rate,* c *is the amplitude of a periodic signal with angular frequency* $\omega = 2\pi f$*. Frequencies considered in this analysis are annual (*$f = 1$ *cpy) and semi-annual (*$f = 2$ *cpy). The reference epoch* t_0 *is set to January 1 2005. Units are* μas *for polar motion components and* $\mu as/d$ *for polar motion rate.* UT *and* LOD *are expressed in* $\mu s/day$*. The RMS's reported in the last column are computed after the removal of linear trends and seasonal terms and expressed in* μas *and* $\mu as/day$*.*

		$Bias$	$Rate$	$Annual$	$Semi-Annual$	RMS
x_p	JTRF	26.30 (0.27)	-3.21 (0.07)	9.85 (0.21)	2.59 (0.21)	14.94
	DTRF	-7.51 (5.24)	3.81 (0.99)	9.30 (0.30)	2.23 (0.28)	17.00
y_p	JTRF	23.05 (0.26)	5.35 (0.07)	17.86 (0.27)	8.00 (0.27)	16.31
	DTRF	-9.40 (5.11)	2.99 (0.96)	5.39 (0.24)	1.70 (0.23)	12.10
UT	JTRF	-2.73 (0.11)	0.31 (0.02)	1.18 (0.06)	0.11 (0.07)	8.94
	DTRF	-2.18 (4.40)	0.28 (0.85)	1.28 (0.40)	1.46 (0.40)	15.90
$\dot{x}_p$	JTRF	0.30 (0.73)	-0.22 (0.15)	2.12 (0.31)	0.99 (0.30)	17.53
	DTRF	-0.69 (3.95)	-0.91 (0.79)	5.37 (2.04)	3.88 (2.05)	117.14
$\dot{y}_p$	JTRF	0.43 (0.72)	-0.07 (0.14)	1.67 (0.31)	0.60 (0.30)	18.62
	DTRF	1.20 (3.87)	0.88 (0.78)	2.48 (2.11)	4.36 (2.10)	117.21
LOD	JTRF	-0.05 (0.22)	0.02 (0.04)	0.13 (0.10)	0.08 (0.10)	13.72
	DTRF	6.13 (3.58)	-0.58 (0.71)	3.17 (4.15)	4.08 (4.26)	142.49

Table 9: *Least-square fits of the EOP differences to COMB2016 [21]. Same conventions as those of Table 8 are applied here.*

		$Bias$	$Rate$	$Annual$	$Semi-Annual$	RMS
x_p	ITRF	3.86 (0.68)	-0.85 (0.14)	9.27 (0.82)	1.06 (0.81)	51.13
	JTRF	32.89 (0.73)	-4.11 (0.16)	8.02 (0.79)	4.50 (0.77)	48.67
	DTRF	-17.16 (5.52)	5.90 (1.06)	6.62 (1.09)	8.83 (1.04)	52.46
y_p	ITRF	2.40 (0.58)	-1.44 (0.12)	1.17 (0.72)	4.95 (0.71)	44.83
	JTRF	25.96 (0.64)	2.79 (0.14)	18.36 (0.69)	6.74 (0.67)	43.54
	DTRF	-3.89 (5.31)	1.34 (1.01)	8.29 (1.05)	9.12 (1.01)	43.89

Table 10: *Observational contributions to combined (multi-technique) Earth Orientation Parameters for each of three TRF products. Bulletted cells in the double-entry table indicate which of the EOP parameters observed by which of the four SG techniques were used in ITRF, JTRF, and DTRF. For instance, the bullet in the row UT-JTRF, column R specifies that UT from VLBI (R) was used when constructing JTRF2014.*

		P	R	L	D
(x_p, y_p)	ITRF	•	•	•	•
	JTRF	•	•	•	•
	DTRF	•	•	•	•
UT	ITRF		•		
	JTRF		•		
	DTRF		•		
$(\dot{x}_p, \dot{y}_p)$	ITRF	•	•		
	JTRF	•	•		
	DTRF	•	•		
LOD	ITRF		•		
	JTRF		•		
	DTRF	•	•	•	

Table 11: *TCH-based estimates of the uncertainty (i.e. square root of the variance associated with the process noise) characterizing the 3 Earth Orientation time series from ITRF, DTRF and JTRF. The first row reports the number of common observations per EOP used in the estimation process. Values reported in the Table are standard deviations whose units are μas for the pole coordinates, $\mu s/d$ for UT and LOD and $\mu as/d$ for polar motion rates. TCH estimates shown here are based on Earth orientation time series spanning the time window 1998.0-2015.0.*

	x_p	y_p	UT	$\dot{x}_p$	$\dot{y}_p$	LOD
OBS	6212	6212	2323	6208	6208	2323
ITRF	18.66	19.93	7.21	11.87	12.13	9.32
JTRF	26.74	23.15	5.50	12.98	14.21	10.06
DTRF	30.23	14.15	14.30	116.74	116.80	142.26

Table 12: *Estimates of the parameters (σ, ϕ) of the AR(1) process of Equation 10, based on a Bayesian fit of Equation 11, adopted to describe the empirical power spectral density of polar motion observations from COMB2016 [21], ITRF2014-, JTRF2014-, DTRF2014-derived EOPs. The estimates reported are median values sampled from the posterior distribution. Parenthesized are 15.73-th and 84-th percentiles, respectively. Units for σ are μas. ϕ is dimensionless.*

	σ	ϕ	χ^2/dof
COMB	17.1586 (-0.0014,0.0009)	0.9977 (-0.0129,0.0103)	1.0002
ITRF	16.1254 (-0.0014,0.0010)	0.9975 (-0.0151,0.0138)	0.9998
JTRF	15.4620 (-0.0015,0.0010)	0.9975 (-0.0157,0.0143)	0.9998
DTRF	12.7757 (-0.0022,0.0014)	0.9974 (-0.0255,0.0244)	1.0000

References

[1] Altamimi, Z., Collilieux, X., Legrand, J., Garayt, B., and Boucher, C. (2007). ITRF2005: A new release of the International Terrestrial Reference Frame based on time series of station positions and Earth Orientation Parameters. J Geophys Res-Sol Ea, 112, B09401.

[2] Altamimi, Z., Collilieux, X., and Métivier, L. (2011). ITRF2008: an improved solution of the International Terrestrial Reference Frame. J Geodesy, (8), 457–473.

[3] Altamimi, Z., Rebischung, P., Métivier, L., and Collilieux, I. (2016). ITRF2014: A new release of the International Terrestrial Reference Frame modeling nonlinear station motions. J Geophys Res-Sol Ea, 121(8), 6109–6131.

[4] Appleby, G., Rodríguez, J., and Altamimi, Z. (2016). Assessment of the accuracy of global geodetic satellite laser ranging observations and estimated impact on ITRF scale: estimation of systematic errors in LAGEOS observations 1993–2014. J Geodesy, 90(12), 1371–1388.

[5] Bachmann, S., Thaller, D., Roggenbuck, O., Lösler, M., and Messerschmitt, L. (2016). IVS contribution to ITRF2014. J Geodesy, 90(7), 631–654.

[6] Bizouard, C., Lambert, S., Becker, O., and Richard, I. Y. (2017). Combined solution C04 for Earth Rotation Parameters consistent with International Terrestrial Reference Frame 2014. Available on-line at the following URL https://hpiers.obspm.fr/iers/eop/eopc04/C04.guide.pdf On-line Accessed 4 August 2017.

[7] Blewitt, G., Heflin, M. B., Webb, F. H., Lindqwister, U. J., and Malla, R. P. (1992). Global coordinates with centimeter accuracy in the International Terrestrial Reference Frame using GPS. Geophys Res Lett, 19(9), 853–856.

[8] Bloßfeld, M., Müller, H., Gerstl, M., Štefka, V., Bouman, J., Göttl, F., and Horwath, M. (2015). Second-degree Stokes coefficients from multi-satellite SLR. J Geodesy, 89(9), 857–871.

[9] Chin, T. M., Gross, R. S., and Dickey, J. O. (2004). Modeling and forecast of the polar motion excitation functions for short-term polar motion prediction. J Geodesy, 78(6), 343–353.

[10] Davis, J. L., Wernicke, B. P., and Tamisiea, M. E. (2012). On seasonal signals in geodetic time series. J Geophys Res-Sol Ea, 117.

[11] Dobslaw, H., Flechtner, F., Bergmann-Wolf, I., Dahle, C., Dill, R., Esselborn, S., Sasgen, I., and Thomas, M. (2013). Simulating high-frequency atmosphere-ocean mass variability for dealiasing of satellite gravity observations: AOD1B RL05. J Geophys Res-Sol Ea, 118(7), 3704–3711.

[12] Fukumori, I., Raghunath, R., Fu, L. L., and Chao, Y. (1999). Assimilation of TOPEX/Poseidon altimeter data into a global ocean circulation model: How good are the results? J Geophys Res-Oceans, 104(C11), 25647–25665.

[13] Haines, B. J., Bar-Sever, Y. E., Bertiger, W. I., Desai, S. D., Harvey, N., Sibois, A. E., and Weiss, J. P. (2015). Realizing a terrestrial reference frame using the Global Positioning System. J Geophys Res-Sol Ea, 120(8), 5911–5939. 2015JB012225.

[14] Han, D. and Wahr, J. (1995). The viscoelastic relaxation of a realistically stratified earth, and a further analysis of postglacial rebound. Geophys J Int, 120(2), 287–311.

[15] Lavallée, D. A., van Dam, T., Blewitt, G., and Clarke, P. J. (2006). Geocenter motions from GPS: A unified observation model. J Geophys Res-Sol Ea, 111(B5). B05405.

[16] Luceri, V. and Pavlis, E. (2016). The ILRS contribution to ITRF2014. Int Laser Rang Serv, Greenbelt, MD, http://itrf.ign.fr/ITRF_solutions/2014/doc/ILRS-ITRF2014-description.pdf. On-line Accessed 4 August 2017.

[17] Moreaux, G., Lemoine, F. G., Capdeville, H., Kuzin, S., Otten, M., Štefánek, P., Willis, P., and Ferrage, P. (2016). The International DORIS Service contribution to the 2014 realization of the International Terrestrial Reference Frame. Adv Space Res, 58(12), 2479–2504.

[18] Percival, D. B. and Walden, A. T. (1993). Spectral Analysis for Physical Applications: Multitaper and Conventional Univariate Techniques. Cambridge University Press.

[19] Petit, G. and Luzum, B. (2010). IERS Conventions (2010), pages 1–179. International Earth Rotation and Reference Systems Service, Central Bureau, Bundesamt für Kartographie und Geodäsie, Richard-Strauss-Allee 11, 60598 Frankfurt am Main, Germany. IERS Technical Note, No. 36.

[20] Premoli, A. and Tavella, P. (1993). A Revisited Three-Cornered Hat Method For Estimating Frequency Standard Instability. IEEE Trans Instrum Meas, 42(1), 7–13.

[21] Ratcliff, J. T. and Gross, R. S. (2017). Combinations of Earth Orientation Measurements: SPACE2016,COMB2016 and POLE2016. JPL Publication 17-8.

[22] Ray, J. and Altamimi, Z. (2005). Evaluation of co-locations ties relating the VLBI and GPS reference frames. J Geodesy, 79(4-5), 189–195.

[23] Ray, J., Kouba, J., and Altamimi, Z. (2005). Is there utility in rigorous combination of VLBI and GPS Earth orientation parameters? J Geodesy, 79, 505–511.

[24] Ray, J., Altamimi, Z., van Dam, T., and Herring, T. (2007). Principles for conventional contributions to modeled station displacements. IERS Conventions Workshop 2007.

[25] Ray, J. R. (1996). Measurements of length of day using the global positioning system. J Geophys Res-Sol Ea, 101(B9), 20141–20149.

[26] Rebischung, P., Altamimi, Z., and Springer, T. (2014). A collinearity diagnosis of the GNSS geocenter determination. J Geodesy, 88(1), 65–85.

[27] Rebischung, P., Altamimi, Z., Ray, J., and Garayt, B. (2016). The IGS contribution to ITRF2014. J Geodesy, pages 1–20.

[28] Rodell, M., Houser, P. R., Jambor, U., Gottschalck, J., Mitchell, K., Meng, C. J., Arsenault, K., Cosgrove, B., Radakovich, J., Bosilovich, M., Entin, J. K., Walker, J. P., Lohmann, D., and Toll, D. (2004). The Global Land Data Assimilation System. B Am Meterol Soc, 85(3), 381–394.

[29] Rudenko, S., Bloßfeld, M., Müller, H., Dettmering, D., Angermann, D., and Seitz, M. (2018). Evaluation of DFTR2014, ITRF2014 and JTRF2014 by Precise Orbit Determination of SLR Satellites. IEEE Transactions on Geoscience and Remote Sensing, 56(6), 3148–3158, 10.1109/TGRS.2018.2793358.

[30] Sarti, P., Abbondanza, C., Petrov, L., and Negusini, M. (2011). Height bias and scale effect induced by antenna gravitational deformations in geodetic VLBI data analysis. J Geodesy, 85(1), 1–8.

[31] Seitz, M., Angermann, D., Bloßfeld, M., Drewes, H., and Gerstl, M. (2012). The 2008 DGFI realization of the ITRS: DTRF2008. J Geodesy, 86(12), 1097–1123.

[32] Seitz, M. and Bloßfeld, M. and Angermann, D. and Schmid, R. and Gerstl, M. and Seitz, F. (2016). The new DGFI-TUM realization of the ITRS: DTRF2014 (data).

[33] Shumway, R.H. and Stoffer, D.S. (2017). Time Series Analysis and Its Applications. Springer Text in Statistics. Springer. Fourth Edition.

[34] Sillard, P. and Boucher, C. (2001). A review of algebraic constraints in terrestrial reference frame datum definition. J Geodesy, 75, 63–73.

[35] Soja, Benedikt and Gross, R. S. and Abbondanza, C. and Chin, T. M. and Heflin, M. B. and Parker, J. W. and Wu, X. and Nilsson, T. and Glaser, S. and Balidakis,K. and Heinkelmann, R. and Schuh, H. (2018). On the long-term stability of terrestrial reference frame solutions based on Kalman filtering. J Geod, 92(9), 1063ï¿½-1077.

[36] van Dam, T. M., Wahr, J., Chao, Y., and Leuliette, E. (1997). Predictions of crustal deformation and of geoid and sea-level variability caused by oceanic and atmospheric loading. Geophys J Int, 129(3), 507–517.

[37] Wu, X. and Heflin, M. B. (2015). A global assessment of accelerations in surface mass transport. Geophys Res Lett, 42(16), 6716–6723, 2015GL064941.

[38] Wu, X., Abbondanza, C., Altamimi, Z., Chin, T. M., Collilieux, X., Gross, R. S., Heflin, M. B., Jiang, Y., and Parker, J. W. (2015). KALREF – A Kalman Filter and Time Series Approach to the International Terrestrial Reference Frame Realization. J Geophys Res-Sol Ea, 120(5), 3775–3802.

[39] Zelensky, N. P., Lemoine, F. G., Beckley, D. B., Chinn, D. S., and Pavlis, D. (2017). Impact of ITRS 2014 Realizations on Altimeter Satellite Precise Orbit Determination. Adv Space Res, 61(1), 45–73.

Appendix 1 JTRF2014 Terrestrial Tie and Space Geodesy Discrepancies

JTRF2014 discrepancies between Space Geodesy and Local ties expressed in mm in the local geodetic frame (ENU). The code outputs differences (Space Geodesy – Local Ties). Also values are in the order ENU, expressed in millimiters. Column 10 and 12 report the SG techniques involved in the tie vectors, with the usual code conventions adopted throughout the manuscript (P is GNSS, R is VLBI, L is SLR, D is DORIS). The asterisks in the last column mark discrepancies larger than 5.0 mm whereas the dashes indicate residuals smaller than 5.0 mm (for instance, the combination '*-*' indicates discrepancies larger than 5.0 mm on the East and Height components, and smaller than 5.0 mm on the North one.)

```
---------------------------------------------------------------------------------------
     From                To
------------------- -------------------
ID   DOMES     SOLN ID   DOMES    SOLN     East  North  Height    SG Tec  Epoch
                                           [mm]   [mm]   [mm]
---------------------------------------------------------------------------------------
QUIN 40433M004    1 7109 40433M002   1    -12.6   19.0   34.2    P -> L  1985.6753 ***
VNDP 40420M007    1 7223 40420M002   1      0.3   -1.1   -1.1    P -> R  1991.9247 ---
SANT 41705M003    1 1404 41705S006   1     -7.3    6.6   13.9    P -> R  1992.5178 ***
GRAZ 11001M002    1 7839 11001S002   1      3.1   -2.1   -6.8    P -> L  1992.8620 --*
PIE1 40456M001    1 7234 40456S001   1     -1.0   -4.8   -3.2    P -> R  1992.9194 ---
7295 40499M002    1 7219 40499S001   1      0.4  -35.9  -12.4    L -> R  1993.0151 -**
7295 40499M002    1 RIDA 40499S016   1      1.7   -6.2   33.5    L -> D  1993.0151 -**
NLIB 40465M001    1 7612 40465S001   1     -1.1   -1.5    0.2    P -> R  1993.1685 ---
MD01 40442M012    1 7080 40442M006   1      1.7    1.0   31.4    P -> L  1993.2068 --*
MD01 40442M012    1 7216 40442S003   1     -7.6  -18.2   20.6    P -> R  1993.2068 ***
MD01 40442M012    1 7613 40442S017   1      5.2   -8.4   23.5    P -> R  1993.2068 ***
KOSG 13504M003    1 8833 13504M002   1     11.1  -25.2    9.9    P -> L  1993.2836 ***
FORT 41602M001    1 7297 41602S001   1     -2.1   -1.7    1.1    P -> R  1993.7247 ---
```

GUAM	50501M002	1	GUAB	50501S001	1	12.8	2.6	15.5	P -> D	1993.9548	*-*
BOR1	12205M002	1	7811	12205S001	1	0.2	2.1	-12.0	P -> L	1994.0315	--*
CRO1	43201M001	1	7615	43201S001	1	0.8	1.4	3.9	P -> R	1994.0507	---
POTS	14106M003	1	7836	14106S009	1	6.5	-1.1	28.4	P -> L	1994.6068	*-*
POTS	14106M003	1	7841	14106S011	1	-15.7	-2.1	10.3	P -> L	1994.6068	*-*
AREQ	42202M005	1	7403	42202M003	1	-4.4	6.3	11.1	P -> L	1995.0096	-**
AREQ	42202M005	1	AREA	42202S005	1	-16.5	-8.7	44.4	P -> D	1995.0096	***
CAGL	12725M003	1	7545	12725M002	1	8.8	18.7	20.6	P -> L	1995.4315	***
CAGL	12725M003	1	CAGZ	12725M004	1	2.3	-3.9	8.9	P -> P	1995.4315	--*
TIDB	50103M108	1	7843	50103S007	1	-10.9	4.2	-42.4	P -> L	1995.7192	*-*
TIDB	50103M108	1	1545	50103S010	1	1.8	4.3	1.4	P -> R	1995.7192	---
TIDB	50103M108	1	ORRA	50103S201	1	-35.4	-26.6	-47.0	P -> D	1995.7192	***
TIDB	50103M108	1	ORRB	50103S202	1	-20.9	-15.2	-58.1	P -> D	1995.7192	***
ZIMM	14001M004	2	7810	14001S001	1	2.8	-3.7	0.4	P -> L	1996.2555	---
MKEA	40477M001	1	7617	40477S001	1	-2.0	0.8	1.7	P -> R	1996.5997	---
GOMA	40405S005	1	GOMB	40405S037	1	4.4	5.8	0.3	D -> D	1996.6571	-*-
WES2	40440S020	2	7205	40440S002	1	9.8	2.1	0.8	P -> R	1996.7527	*--
WES2	40440S020	2	7209	40440S003	1	2.0	-1.8	13.5	P -> R	1996.7527	--*
SANT	41705M003	2	SANA	41705S007	1	2.8	14.3	-16.7	P -> D	1996.9249	-**
SANT	41705M003	2	SAOB	41705S008	1	6.9	-1.1	9.7	P -> D	1996.9249	*-*
SANT	41705M003	2	SANB	41705S009	1	-22.6	0.9	16.8	P -> D	1996.9249	*-*
MADR	13407S012	7	1565	13407S010	1	-52.5	17.5	-1.3	P -> R	1998.9959	**-
ALGO	40104M002	1	7282	40104S001	1	-1.7	-2.3	13.4	P -> R	1998.9959	--*
NKLG	32809M002	1	LIBA	32809S002	1	13.7	-4.7	0.3	P -> D	1999.0918	*--
NKLG	32809M002	1	LIBB	32809S003	1	5.0	5.7	-0.8	P -> D	1999.0918	**-
CHAT	50207M001	1	CHAB	50207S001	1	-3.7	1.9	6.7	P -> D	1999.1493	--*
STJO	40101M001	3	STJB	40101S002	1	3.1	-0.7	7.7	P -> D	1999.7438	--*
MONP	40497M004	1	7110	40497M001	3	3.2	1.7	1.4	P -> L	1999.7630	---
KGNI	21704S005	1	7308	21704S002	1	-5.4	3.0	71.1	P -> L	1999.7822	*-*
KGNI	21704S005	1	7328	21704M001	1	-4.6	-0.6	57.2	P -> L	1999.7822	--*
GRAS	10002M006	1	7835	10002S001	1	2.2	0.0	-3.6	P -> L	1999.7822	---
GRAS	10002M006	1	7845	10002S002	1	-0.6	0.6	7.3	P -> L	1999.7822	--*
KSMV	21701S007	1	1856	21701S001	1	1.8	15.1	98.3	P -> R	1999.8014	-**
KSMV	21701S007	1	1857	21701S004	1	-0.5	15.2	75.5	P -> R	1999.8014	-**
YEBE	13420M001	1	7333	13420S001	1	2.0	1.4	-34.1	P -> R	1999.8781	--*
SYOG	66006S002	2	SYOB	66006S001	1	-5.4	0.2	-41.7	P -> D	1999.9932	*-*
SYOG	66006S002	2	SYPB	66006S003	1	9.5	11.0	-16.3	P -> D	1999.9932	***
SYOG	66006S002	2	7342	66006S004	1	-6.8	13.0	43.7	P -> R	1999.9932	***
AJAC	10077M005	1	7848	10077M002	1	-9.9	-6.0	17.2	P -> L	1999.9932	***
KSTU	12349M002	1	KRAB	12349S001	1	-4.0	15.5	3.7	P -> D	1999.9932	-*-
LHAS	21613M001	1	LHAZ	21613M002	1	3.3	1.6	-13.8	P -> P	2000.1462	--*
DJIA	39901S002	1	DJIB	39901S003	1	0.0	0.1	-0.2	D -> D	2000.4904	---
DJIA	39901S002	1	DJIB	39901S003	1	0.0	0.1	-0.2	D -> D	2000.4904	---
METS	10503S011	1	META	10503S013	1	-1.0	-0.8	-17.7	P -> D	2000.8156	--*
METS	10503S011	1	METB	10503S015	1	0.1	3.8	-10.0	P -> D	2000.8156	--*

METS	10503S011	1	7806	10503S014	1	-2.0	-6.0	-10.3	P -> L	2000.8156	-**
METS	10503S011	1	METZ	10503M005	1	-0.5	-0.3	-3.9	P -> P	2000.8156	---
BAKO	23101M002	3	CIBB	23101S001	1	-2.8	6.4	54.2	P -> D	2000.9495	-**
BAKO	23101M002	3	CICB	23101S002	1	-15.5	4.9	43.5	P -> D	2000.9495	*-*
RIOG	41507M004	2	RIOA	41507S003	1	7.6	1.3	2.4	P -> D	2001.0452	*--
RIOG	41507M004	2	RIOB	41507S004	1	-3.7	10.8	-13.3	P -> D	2001.0452	-**
RIOG	41507M004	2	RIPB	41507S005	1	-1.9	-1.8	-6.7	P -> D	2001.0452	--*
EISL	41703M003	1	EASB	41703S009	1	9.1	8.2	-5.2	P -> D	2001.1219	***
EISL	41703M003	1	EASA	41703S008	1	-6.5	12.8	-25.5	P -> D	2001.1219	***
EISL	41703M003	1	7097	41703M002	1	-17.6	5.5	14.5	P -> L	2001.1219	***
PDEL	31906M004	1	PDLB	31906S001	1	8.0	9.7	4.8	P -> D	2001.2178	**-
PDEL	31906M004	1	PDMB	31906S002	1	16.5	3.4	-2.2	P -> D	2001.2178	*--
KIT3	12334M001	1	KITA	12334S004	1	-25.5	10.2	-9.6	P -> D	2001.3137	***
KIT3	12334M001	1	KITB	12334S005	1	-10.4	14.0	-2.3	P -> D	2001.3137	**-
KIT3	12334M001	1	KIUB	12334S006	1	10.3	7.7	-3.4	P -> D	2001.3137	**-
SEY1	39801M001	2	MAHB	39801S005	1	-0.3	-1.7	-109.8	P -> D	2001.4096	--*
STR2	50119M001	1	STR1	50119M002	1	-1.6	-1.2	11.5	P -> P	2001.5630	--*
STR2	50119M001	1	MSOB	50119S002	1	-6.0	11.6	16.0	P -> D	2001.5630	***
STR2	50119M001	1	MSPB	50119S004	1	-10.3	2.1	-7.1	P -> D	2001.5630	*-*
STR2	50119M001	1	7849	50119S001	1	-4.4	0.8	6.3	P -> L	2001.5630	--*
STR2	50119M001	1	7825	50119S003	1	-4.6	-4.5	-8.1	P -> L	2001.5630	--*
FAIR	40408M001	3	FAIA	40408S004	1	-7.3	-8.2	-29.8	P -> D	2001.7548	***
FAIR	40408M001	3	FAIB	40408S005	1	14.8	-2.5	-17.7	P -> D	2001.7548	*-*
FAIR	40408M001	3	7225	40408S002	1	-1.3	-6.7	4.2	P -> R	2001.7548	-*-
YELL	40127M003	2	YELB	40127S008	1	5.1	-4.3	-9.3	P -> D	2001.7740	*-*
YELL	40127M003	2	YEMB	40127S009	1	2.4	0.4	-9.7	P -> D	2001.7740	--*
YELL	40127M003	2	7296	40127M004	1	-2.6	-4.9	-7.7	P -> R	2001.7740	--*
TRIA	30604S001	1	TRIB	30604S002	1	4.3	-5.1	-17.9	D -> D	2002.0616	-**
OHI2	66008M005	1	7245	66008S001	1	-0.8	3.7	2.1	P -> R	2002.1192	---
HOB2	50116M004	1	7242	50116S002	1	6.1	-1.2	-0.3	P -> R	2002.2151	*--
MORA	51001S001	1	MORB	51001S002	1	-15.2	9.9	3.8	D -> D	2002.2151	**-
ADEA	91501S001	1	ADEB	91501S002	1	-8.6	-5.4	22.9	D -> D	2002.2918	***
ONSA	10402M004	3	7213	10402S002	1	7.6	0.2	-3.2	P -> R	2002.5219	*--
THU2	43001M002	1	THUB	43001S005	1	28.8	8.6	4.8	P -> D	2002.6945	**-
KOKB	40424M004	3	KOLB	40424S009	1	1.4	12.1	-24.9	P -> D	2002.8671	-**
KOKB	40424M004	3	KOKA	40424S008	1	10.7	10.9	-17.1	P -> D	2002.8671	***
KOKB	40424M004	3	1311	40424S001	1	15.6	39.2	4.3	P -> R	2002.8671	**-
KOKB	40424M004	3	7298	40424S007	1	16.8	38.6	-4.8	P -> R	2002.8671	**-
MANA	22006S001	1	MANB	22006S002	1	3.6	-20.2	8.0	D -> D	2003.1548	-**
HELA	30606S002	1	HELB	30606S003	1	17.1	3.5	-16.2	D -> D	2003.2123	*-*
HELA	30606S002	1	HEMB	30606S004	1	15.4	1.2	-10.7	D -> D	2003.2123	*-*
CONZ	41719M002	1	7405	41719M001	1	3.5	-4.7	21.4	P -> L	2003.2123	--*
CONZ	41719M002	1	7640	41719S001	1	3.3	-3.4	29.5	P -> R	2003.2123	--*
BJFS	21601M001	2	7249	21601S004	1	-1.5	9.1	-4.2	P -> L	2003.4616	-*-
HRAO	30302M004	1	7232	30302S001	1	3.9	0.3	1.7	P -> R	2003.5767	---

HRAO	30302M004	1	7501	30302M003	1	-0.1	6.8	1.9	P -> L	2003.5767	-*-
HRAO	30302M004	1	HARB	30302M009	1	2.6	2.3	0.6	P -> P	2003.5767	---
HRAO	30302M004	1	HBKB	30302S006	1	4.9	6.6	-2.6	P -> D	2003.5767	-*-
HRAO	30302M004	1	HBKA	30302S202	1	-1.6	-5.0	-16.9	P -> D	2003.5767	-**
HRAO	30302M004	1	HBLA	30302S005	1	0.4	2.7	-20.2	P -> D	2003.5767	--*
NYA1	10317M003	2	SPIA	10317S002	1	-2.0	-1.7	-13.5	P -> D	2003.6151	--*
NYA1	10317M003	2	SPIB	10317S004	1	-2.9	1.3	-1.1	P -> D	2003.6151	---
NYA1	10317M003	2	SPJB	10317S005	1	0.1	-3.6	-12.8	P -> D	2003.6151	--*
NYA1	10317M003	2	7331	10317S003	1	4.2	-1.8	1.4	P -> R	2003.6151	---
YAR1	50107M004	2	YARR	50107M006	1	-0.6	1.9	0.8	P -> P	2003.8260	---
YAR1	50107M004	2	7090	50107M001	1	-4.2	4.6	14.2	P -> L	2003.8260	--*
YAR1	50107M004	2	YARB	50107S010	1	1.2	21.7	19.4	P -> D	2003.8260	-**
YAR1	50107M004	2	YASB	50107S011	1	-7.2	13.6	21.6	P -> D	2003.8260	***
AMSA	91401S001	1	AMTB	91401S003	1	1.9	2.6	2.2	D -> D	2003.8836	---
SHAO	21605M002	1	7837	21605S001	1	0.0	0.4	-15.7	P -> L	2003.9027	--*
SHAO	21605M002	1	7227	21605S009	1	3.7	-6.3	1.3	P -> R	2003.9027	-*-
REUN	97401M003	2	REUA	97401S001	1	-7.6	7.7	0.9	P -> D	2003.9219	**-
REUN	97401M003	2	REUB	97401S002	1	-3.9	9.9	2.1	P -> D	2003.9219	-*-
WUHN	21602M001	5	JIUB	21602S005	1	-7.1	-12.6	-12.5	P -> D	2003.9411	***
ASC1	30602M001	1	ASDB	30602S004	1	30.1	6.9	-15.0	P -> D	2003.9603	***
TLSE	10003M009	1	TLHA	10003S003	1	4.3	-4.0	-13.6	P -> D	2004.0943	--*
TLSE	10003M009	1	TLSA	10003S001	1	-3.3	8.4	-4.7	P -> D	2004.0943	-*-
CHPI	41609M003	1	CACB	41609S001	1	-18.9	10.0	-11.8	P -> D	2004.2281	***
CHPI	41609M003	1	CADB	41609S002	1	4.1	4.0	-95.5	P -> D	2004.2281	--*
BADA	12338S001	1	BADB	12338S002	1	-0.7	-0.4	0.1	D -> D	2004.6107	---
YSSK	12329M003	3	SAKA	12329S001	2	-16.6	2.0	-7.5	P -> D	2004.6298	*-*
YSSK	12329M003	3	SAKB	12329S002	1	-1.2	2.5	1.1	P -> D	2004.6298	---
MARA	30313S001	1	MARB	30313S002	1	-13.3	26.0	3.5	D -> D	2004.6489	**-
MARA	30313S001	1	MATB	30313S003	1	0.3	-24.4	-4.9	D -> D	2004.6489	-*-
REYK	10202M001	6	REYA	10202S001	1	-7.7	-18.3	-43.2	P -> D	2004.6680	***
REYK	10202M001	6	REYB	10202S002	1	-4.3	-4.4	-5.0	P -> D	2004.6680	---
REYK	10202M001	6	REZB	10202S003	1	8.5	-7.7	-1.4	P -> D	2004.6680	**-
MATE	12734M008	3	7243	12734S005	1	-0.3	-4.1	-1.2	P -> R	2004.8210	---
MATE	12734M008	3	7941	12734S008	1	0.5	-0.3	-5.8	P -> L	2004.8210	--*
SVTL	12350M001	2	7380	12350S001	1	-3.6	-9.3	-12.6	P -> R	2004.9932	-**
ZECK	12351M001	1	7381	12351S001	1	-19.9	0.6	24.5	P -> R	2004.9932	*-*
MALD	22901S001	3	MALB	22901S002	1	-3.8	-9.1	-0.5	P -> D	2005.0315	-*-
AOML	49914S001	2	MIAB	49914S003	1	6.7	1.6	-3.0	P -> D	2005.0890	*--
ROTA	66007S001	1	ROTB	66007S002	1	0.1	-0.1	-1.0	D -> D	2005.1466	---
GLPS	42005M002	1	SCRB	42005S001	1	0.1	3.4	5.5	P -> D	2005.2425	--*
NOUM	92701M003	3	NOUB	92701S002	1	-0.6	12.5	13.3	P -> D	2005.6452	-**
NOUM	92701M003	3	NOWB	92701S003	1	-2.3	21.4	19.1	P -> D	2005.6452	-**
NOUM	92701M003	3	NOUA	92701S001	1	-5.6	6.5	-9.5	P -> D	2005.6452	***
NOT1	12717M004	2	7547	12717S001	1	-0.5	-1.5	8.2	P -> R	2005.7219	--*
MONP	40497M004	3	MONB	40497S008	1	6.2	-0.7	2.5	P -> D	2005.9137	*--

MONP	40497M004	3	MOOB	40497S009	1	-0.7	-1.4	-0.7	P -> D	2005.9137	---
BRFT	41602M002	1	7297	41602S001	1	1.1	-4.3	8.4	P -> R	2006.2205	--*
DIOB	12602S012	1	DIOA	12602S011	1	-2.4	-9.3	0.3	D -> D	2006.3740	-*-
MAUI	40445S008	2	7119	40445M004	1	1.3	4.6	-15.7	P -> L	2006.7192	--*
MAUI	40445S008	2	7210	40445M001	3	3.4	1.6	-18.9	P -> L	2006.7192	--*
CROB	91301S001	1	CRPB	91301S002	1	-1.2	0.2	-1.6	D -> D	2007.2562	---
KERG	91201M002	3	KERB	91201S003	1	-1.6	6.7	1.3	P -> D	2007.2753	-*-
KERG	91201M002	3	KESB	91201S004	1	8.7	10.0	15.2	P -> D	2007.2753	***
KERG	91201M002	3	KETB	91201S005	1	4.9	18.5	5.1	P -> D	2007.2753	-**
AMTB	91401S003	1	AMUB	91401S004	1	-2.5	0.5	-2.1	D -> D	2007.2945	---
MEDI	12711M003	4	7230	12711S001	1	5.1	-0.2	2.8	P -> R	2007.6589	*--
THTI	92201M009	1	7124	92201M007	1	-2.8	-2.9	-1.8	P -> L	2007.7548	---
THTI	92201M009	1	PAPB	92201S007	1	6.3	-16.1	17.9	P -> D	2007.7548	***
THTI	92201M009	1	PAQB	92201S008	1	-4.3	-2.3	12.6	P -> D	2007.7548	--*
THTI	92201M009	1	PATB	92201S010	1	-5.0	-1.8	11.8	P -> D	2007.7548	*-*
GODE	40451M123	2	7105	40451M105	2	0.8	5.0	-5.6	P -> L	2008.0041	--*
GODE	40451M123	2	GREB	40451S176	1	8.1	-4.9	-13.8	P -> D	2008.0041	*-*
TSKB	21730S005	6	7345	21730S007	1	-2.1	0.9	8.3	P -> R	2008.0423	--*
DUM1	91501M001	3	ADEA	91501S001	1	0.2	3.0	-13.7	P -> D	2008.0997	--*
DUM1	91501M001	3	ADFB	91501S003	1	-6.7	0.2	7.2	P -> D	2008.0997	*-*
HERS	13212M007	4	HERT	13212M010	2	0.2	-2.9	-6.1	P -> P	2008.4822	--*
HERS	13212M007	4	7840	13212S001	1	-0.3	-1.9	-8.1	P -> L	2008.4822	--*
GRAS	10002M006	2	7845	10002S002	1	-4.0	-2.5	-4.9	P -> L	2009.6507	---
GRAS	10002M006	2	GR3B	10002S018	1	6.6	-8.9	4.3	P -> D	2009.6507	**-
STR1	50119M002	2	MSPB	50119S004	1	-8.7	8.8	-9.5	P -> D	2009.8616	***
STR1	50119M002	2	7825	50119S003	1	-6.0	-1.5	-18.5	P -> L	2009.8616	*-*
HOB2	50116M004	2	7242	50116S002	1	2.0	-1.4	-1.7	P -> R	2009.9000	---
HOB2	50116M004	2	7374	50116S007	1	5.2	1.9	3.0	P -> R	2009.9000	*--
NKLG	32809M002	3	LICB	32809S004	1	-9.8	-8.1	25.6	P -> D	2010.3411	***
ASDB	30602S004	1	ASEB	30602S005	1	32.3	-15.8	0.2	D -> D	2010.4562	**-
YAR1	50107M004	2	YARR	50107M006	1	-0.5	1.0	-1.1	P -> P	2010.5521	---
YAR1	50107M004	2	7090	50107M001	2	-7.5	1.3	6.6	P -> L	2010.5521	*-*
YAR1	50107M004	2	YASB	50107S011	1	-6.7	11.8	21.4	P -> D	2010.5521	***
YAR1	50107M004	2	YAR3	50107M008	2	-0.8	1.3	21.4	P -> P	2010.5521	--*
YAR1	50107M004	2	7376	50107S012	1	-7.6	0.0	-12.5	P -> R	2010.5521	*-*
ROTH	66007M003	1	ROTB	66007S002	1	11.1	0.7	-16.8	P -> D	2011.0890	*-*
ROTH	66007M003	1	ROUB	66007S003	1	6.2	3.7	-18.2	P -> D	2011.0890	*-*
ROTH	66007M003	1	ROVB	66007S004	1	0.8	4.6	-9.2	P -> D	2011.0890	--*
KOUG	97301M402	1	KRWB	97301S006	1	0.1	-15.6	23.2	P -> D	2011.1466	-**
KOUG	97301M402	1	KRUB	97301S004	1	-2.5	-21.0	16.4	P -> D	2011.1466	-**
KOUG	97301M402	1	KOUR	97301M210	3	-1.3	-1.9	4.1	P -> P	2011.1466	---
DYNG	12602M006	1	DIOB	12602S012	1	-4.7	-7.1	-4.7	P -> D	2011.3575	-*-
THTI	92201M009	1	PATB	92201S010	1	-4.9	-1.7	11.9	P -> D	2011.3575	--*
KAT1	59968M001	2	7375	59968S001	1	-2.3	0.7	12.0	P -> R	2011.4151	--*
BREW	40473M001	1	7614	40473S001	1	0.3	0.7	5.5	P -> R	2011.5685	--*

RILB	92301S003	1	RIMB	92301S004	1	-0.5	0.8	-0.5	D -> D	2011.5877	---
SOLA	20101M001	1	7832	20101S001	1	-1.5	-2.3	-29.8	P -> L	2012.0861	--*
FTNA	92902S002	3	FUUB	92902S003	1	-8.0	15.8	3.2	P -> D	2012.3730	**-
FTNA	92902S002	3	FUTB	92902S001	1	-17.7	22.7	10.4	P -> D	2012.3730	***
WTZA	14201M013	1	7224	14201S004	1	-5.3	-4.2	-3.9	P -> R	2012.4112	*--
WTZA	14201M013	1	8834	14201S018	1	-8.2	-3.6	4.9	P -> L	2012.4112	*--
WTZA	14201M013	1	WTZJ	14201M012	1	-6.6	-5.5	-1.2	P -> P	2012.4112	**-
WTZA	14201M013	1	WTZR	14201M010	3	-3.5	-0.4	-15.2	P -> P	2012.4112	--*
WTZA	14201M013	1	WTZS	14201M015	3	-4.8	-3.3	-10.4	P -> P	2012.4112	--*
WTZA	14201M013	1	WTZZ	14201M014	2	-2.3	-0.2	-7.5	P -> P	2012.4112	--*
TRIB	30604S002	2	TRJB	30604S003	1	0.0	0.0	0.7	D -> D	2012.4495	---
SEY1	39801M001	4	MAHB	39801S005	1	-11.6	-1.0	20.7	P -> D	2012.4495	*-*
SEY1	39801M001	4	MAIB	39801S006	1	-4.1	3.6	11.7	P -> D	2012.4495	--*
METS	10503S011	6	MEUB	10503S016	1	5.8	-4.7	-1.8	P -> D	2012.5068	*--
METS	10503S011	6	METB	10503S015	1	0.9	-3.3	2.5	P -> D	2012.5068	---
GODE	40451M123	2	7105	40451M105	2	2.8	1.3	-6.5	P -> L	2012.5260	--*
GODE	40451M123	2	7918	40451M120	1	0.6	-2.9	-4.6	P -> L	2012.5260	---
GODE	40451M123	2	GODN	40451M127	1	1.6	1.0	-4.2	P -> P	2012.5260	---
GODE	40451M123	2	GODS	40451M128	1	2.2	1.5	-5.1	P -> P	2012.5260	--*
GODE	40451M123	2	GRFB	40451S178	1	13.2	-2.3	-18.3	P -> D	2012.5260	*-*
WUHN	21602M001	7	JIUB	21602S005	1	-11.6	-6.3	-20.3	P -> D	2012.7746	***
WUHN	21602M001	7	JIVB	21602S006	1	-8.6	4.7	-15.6	P -> D	2012.7746	*-*
AREQ	42202M005	14	ARFB	42202S007	1	16.3	18.9	34.2	P -> D	2013.0233	***
AREQ	42202M005	14	7403	42202M003	5	0.1	0.1	2.1	P -> L	2013.0233	---
OHI2	66008M005	3	OHI3	66008M006	3	1.1	0.5	-4.2	P -> P	2013.1192	---
MDO1	40442M012	5	7080	40442M006	2	-0.3	17.7	-20.8	P -> L	2013.1384	-**
MDO1	40442M012	5	7613	40442S017	1	8.6	18.6	-0.5	P -> R	2013.1384	**-
STJO	40101M001	5	STJB	40101S002	1	4.1	4.7	0.6	P -> D	2013.5219	---
STJO	40101M001	5	STKB	40101S003	1	-12.3	15.4	-7.5	P -> D	2013.5219	***
YELL	40127M003	4	YEMB	40127S009	1	-1.1	4.9	-5.6	P -> D	2013.5411	--*
TLSE	10003M009	2	TLSB	10003S005	1	4.3	-9.6	-12.4	P -> D	2014.1164	-**
HARB	30302M009	2	HBMB	30302S008	1	1.4	8.0	-1.9	P -> D	2014.1548	-*-
HRAO	30302M004	4	7501	30302M003	1	-22.0	8.1	6.6	P -> L	2014.1548	***
HRAO	30302M004	4	7378	30302S009	1	-21.0	4.2	19.5	P -> R	2014.1548	*-*
HRAO	30302M004	4	7232	30302S001	1	-16.7	0.3	15.5	P -> R	2014.1548	*-*
KOKB	40424M004	5	KOLB	40424S009	1	-1.6	-0.6	0.1	P -> D	2014.2123	---
KOKB	40424M004	5	7298	40424S007	1	2.8	3.8	12.6	P -> R	2014.2123	--*
RIO2	41507M006	2	RIRB	41507S007	1	1.0	14.6	-8.5	P -> D	2014.3849	-**
ONSA	10402M004	3	7213	10402S002	1	4.5	0.0	9.1	P -> R	2014.4808	--*
PDEL	31906M004	5	PDMB	31906S002	1	11.4	-12.4	-4.6	P -> D	2014.7301	**-
PTAG	22006M005	1	MANB	22006S002	1	-15.7	6.4	22.2	P -> D	2014.9219	***